Seismic Interpretation of Sill-Complexes in Sedimentary Basins: The 'Sub-Sill Imaging Problem'

Christian Haug Eide[1,], Nick Schofield[2], Isabelle Lecomte[1], Simon J. Buckley[1,3] and John A. Howell[2]*

[1]*Department of Earth Science, University of Bergen, Box 7803, 5020 Bergen, Norway*

[2]*School of Geosciences,* Meston Building, *University of Aberdeen, Aberdeen, AB24 3UE, UK*

[3]*Centre for Integrated Petroleum Research, Uni Research CIPR, Box* 7810, 5020 Bergen, Norway

[*]*Correspondence:* christian.eide@uib.no

This is a ***preprint*** for a manuscript submitted to the *Journal of the Geological Society*, on July 25th 2017

11 997 words, 72 references, 1 table, 13 figures

Running head: Seismic interpretation of sill-complexes

Supplementary materials: None included

Abstract

Application of 3D-seismic reflection-data to igneous systems in sedimentary basins has led to a revolution in the understanding of mafic sill-complexes. However, there is considerable uncertainty on how geometries and architecture of sill complexes within the subsurface relates those imaged in seismic reflection-data. To provide constraints on how sill complexes in seismic data should be interpreted, we present synthetic seismograms generated from a seismic-scale (22x0.25 km) outcrop in East Greenland constrained by abundant field-data.

This study highlights how overlying igneous rocks adversely affect imaging of underlying intrusions and rocks by decreasing seismic amplitude, frequency and making steeply dipping features near-impossible to image. Furthermore, seismic modelling shows that because of the high impedance contrast between siliciclastic host rock and dolerites, thin (< 5m) intrusions should in principle be imaged at relatively high amplitudes. This is contrary to many published 'rules of thumb' for seismic detectability of sill intrusions. However, actual seismic data combined with well-data shows significant amounts of un-imaged sill intrusions, and this is likely due to limited resolution, overburden complexity, poor velocity-models, and interference between closely spaced sill-splays. Significant improvements could be made by better predicting occurrence and geometry of sill intrusions and including these in velocity models.

1. Introduction

Igneous sill intrusions are common at volcanic rifted margins, in rifted basins and in large igneous provinces (e.g. Eldholm and Coffin, 2000; Skogseid, 2001; Bryan and Ferrari, 2013). Understanding the role of, and processes controlling, sills in such systems is essential to understand monitoring of volcanoes (Galland, 2012), understand magma-propagation in the crust and to volcanoes (Cartwright and Hansen, 2006a; Magee et al., 2013; Muirhead et al., 2016) and to understand hydrocarbon systems and plan hydrocarbon exploration in intruded basins (Rateau et al 2013; Schofield et al., 2015, 2016, 2017; Millett et al., 2016; Senger et al., 2017). Because of the high density- and velocity-contrasts between mafic intrusions and sedimentary host rock, intrusions are in principle readily imaged within seismic reflection datasets (e.g. Smallwood and Maresh, 2002). Models and understanding of igneous systems in sedimentary basins have seen significant progress following the application of 3D seismic data to study sill intrusions (e.g. Cartwright and Huuse, 2003; Thomson and Hutton, 2004; Hansen and Cartwright, 2006a; Thomson and Schofield, 2008, Schofield et al. 2012b; Magee et al., 2013; Jackson et al., 2013; Jerram and Bryan, 2015; Schofield et al. 2015). As hydrocarbon exploration moves into increasingly challenging basins, and as oil and gas fields are being targeted and discovered in the vicinity of intrusions (e.g. Tormore; Schofield et al., 2015), it is essential to have a good understanding of how real geometries of intrusions are imaged in the subsurface.

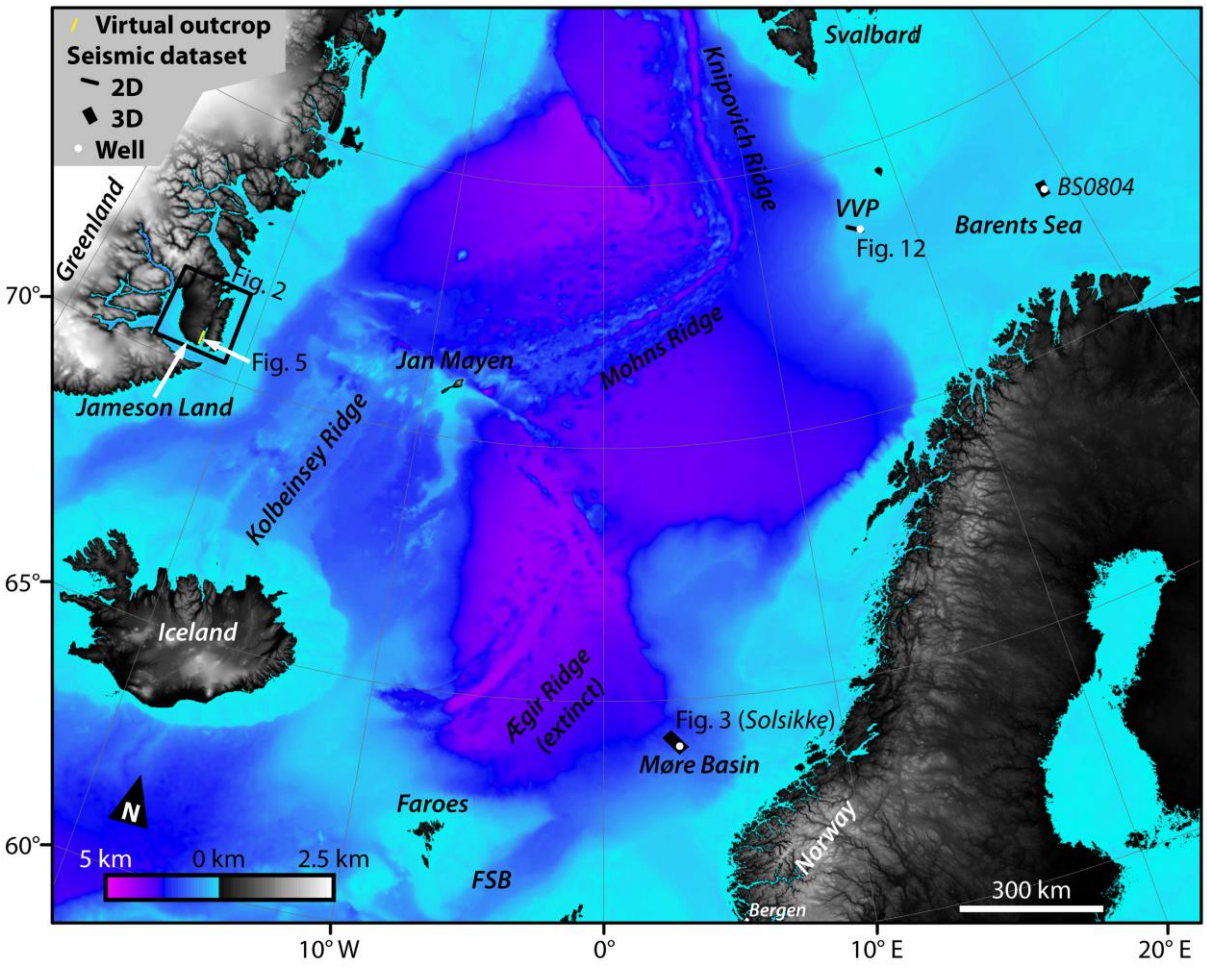

Fig. 1*: Map of the conjugate margins around the Norwegian-Greenland Sea, showing locations of datasets used for this study. FSB, Faroe-Shetland Basin, VVP, Vestbakken Volcanic Province.*

However, studies of large-scale architectures of igneous intrusions are commonly based on seismic data. Studies of architecture of igneous intrusions in outcrops that have a scale comparable to seismic data (100s of m high, tens of km long) are rare, apart from one study by Eide et al (2017, Figs. 1, 2). This is a problem, because it is difficult to know exactly how properties of sill complexes imaged in seismic reflection data relate to actual geometries of sill complexes within the subsurface (Magee et al., 2015). This is an issue due to three inherent limitations in the 3D seismic method (Fig. 3): (1) decrease of seismic quality and resolution with depth due to absorption of high frequencies, seismic energy and downward increase in seismic velocity (e.g. Brown, 2011; Planke et al., 2005); (2)

overburden effects, where the seismic signal is affected by complex overburden which can be a considerable problem in basins with igneous rocks (e.g. Ziolkowski et al., 2003; Gallagher and Dromgoole, 2007; Flecha et al., 2011; Holford et al., 2013; Schofield et al., 2016); and (3) the inability of the reflection seismic method to image steeply dipping and vertical interfaces (e.g. Lecomte et al., 2016). Furthermore, reflection seismic data from areas with sill complexes are commonly not processed in ways that are optimal to preserve important details in such systems.

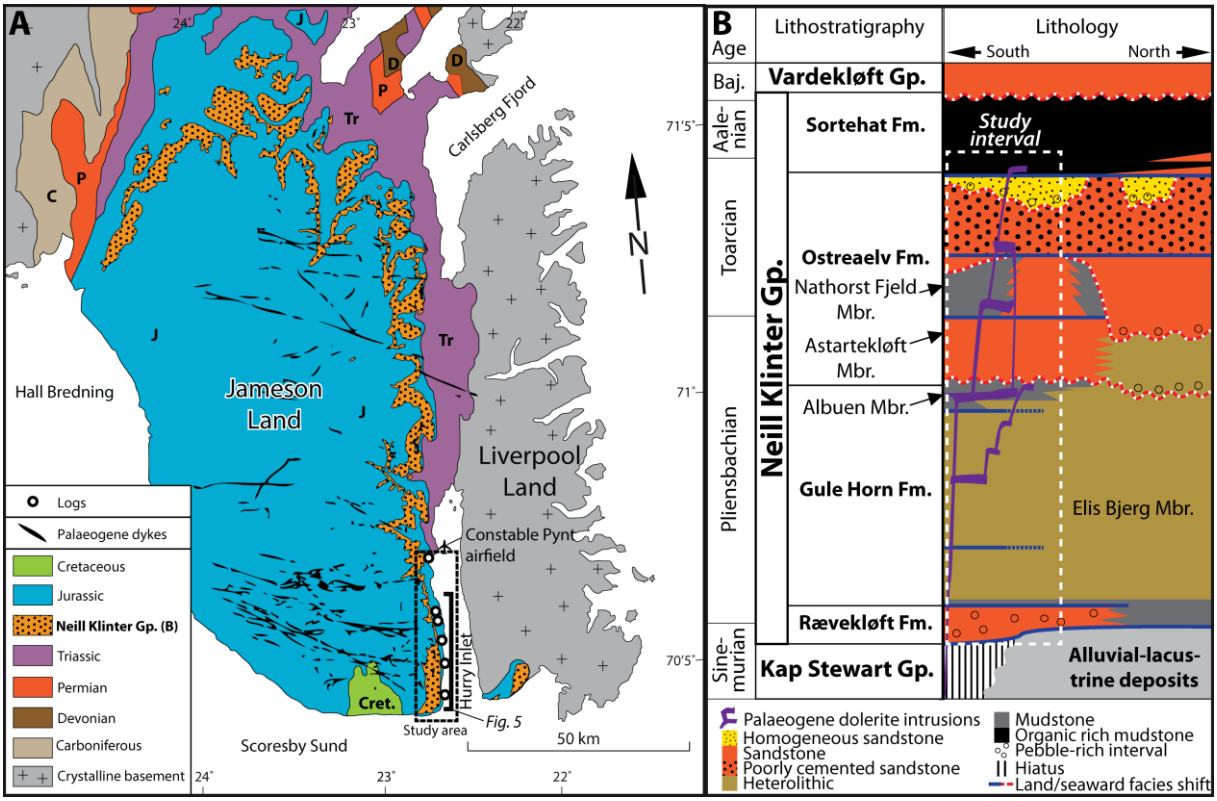

***Fig. 2**: Location and setting of the main outcrop dataset. See Fig. 1 for location. A) Geological map of the study area, modified from Ahokas et al., 2014. Note occurrence and orientation of dykes. B) Lithostratigraphy of the studied Jurassic Neill Klinter Gp. modified from Ahokas et al. (2014) and Eide et al. (2016).*

In this paper, we investigate how an outcropping example of a Paleogene sill complex intruded at c. 3 km depth in Jurassic sedimentary rock (Fig. 2; Eide et al., 2016; Eide et al.,

2017) would be imaged in seismic data at various simulated scenarios. Synthetic seismic data was generated using actual sill geometries, using methods that explicitly model both limited vertical and lateral resolution and take the inability to image steep beds into account (Lecomte et al., 2016). We also compare our results to actual seismic from the conjugate Norwegian Margin (Fig. 1), which has experienced significant volcanism both related to initial opening and during later readjustment (Talwani & Eldholm, 1977; Saunders et al 1997; Faleide et al 2008).

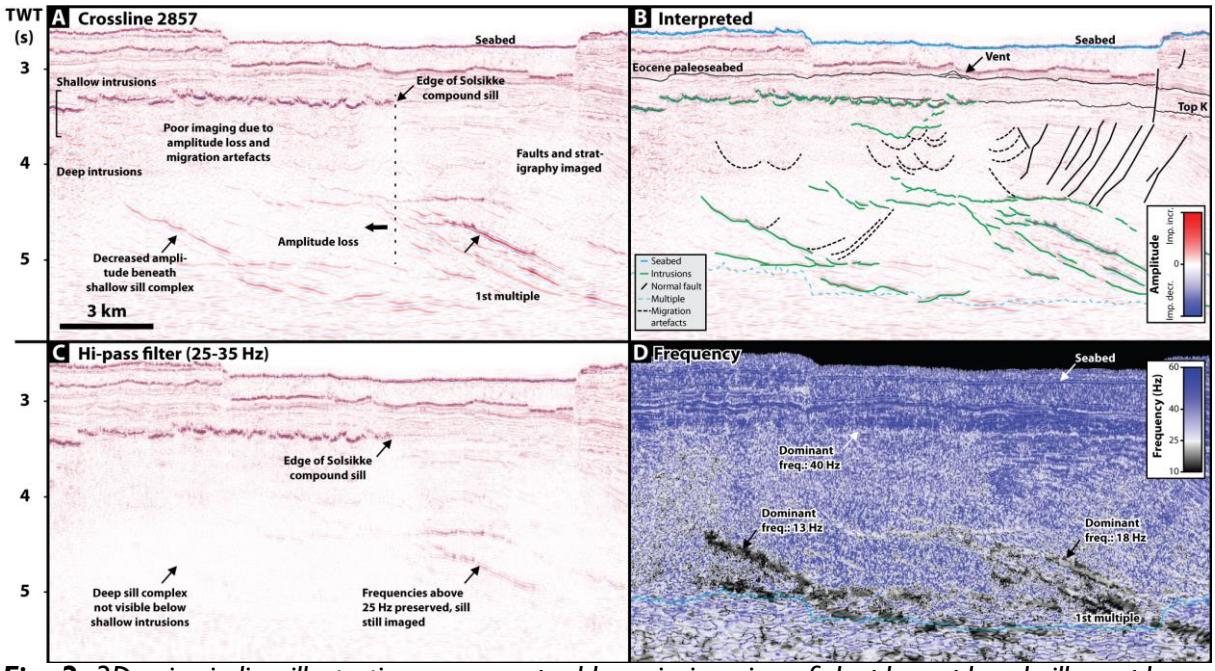

Fig. 3*: 3D seismic line illustrating common problems in imaging of deeply emplaced sill complexes. For location, see Fig. 1. A) Uninterpreted seismic line. Note the shallow intrusions, which mainly appear as compound saucer-shapes, and the deeper intrusions, which show more layer-parallel and branching geometries. Also note the poor imaging below the shallow intrusions, and the general decrease of resolution and definition with depth. B) Interpreted version of A. K, Cretaceous. C) High-pass filtered version of (A) with a filter sloping from 35 to 25 Hz. Note loss of high frequencies below the shallow intrusions. D) Frequency plot of (A). Note the high dominant frequencies in the*

100 *upper part of the survey, lower frequencies in the lower part, and lowest frequencies below the*
101 *shallow sill.*

102 The goals of this study are threefold: (1) To investigate how deeply emplaced sill
103 complexes are imaged in seismic data; (2) to investigate how overburden complexity affect
104 imaging of sill complexes; and (3) to discuss what these results imply for the interpretation
105 of sill complexes in seismic data

106 ## 1.1 Synthetic seismograms of sill complexes - issues and previous work

107 In order to investigate how actual sill geometries would be imaged in seismic data, synthetic
108 seismograms can be generated from actual or conceptual models. Synthetic seismic data are
109 routinely generated by constructing a reflectivity model, extracting one-dimensional (1D)
110 vertical traces along this model, convolving these traces with a wavelet to obtain seismic
111 traces (referred to as 1D convolution), and visualizing these traces as synthetic seismograms
112 (Fig. 4c; e.g. Magee et al., 2015). However, although such methods give a good, first-order
113 impression of seismic imaging in areas of little lateral variation, such methods are unsuited to
114 investigate seismic imaging of complex geology because they vastly overestimate lateral
115 seismic resolution, (e.g. Lecomte et al., 2016), such as in the case of salt diapirs, fold-and-
116 thrust belts, or in this case: igneous sill complexes. The 1D convolution method leads to
117 three particularly noteworthy artefacts that would not be present in actual 'real-world'
118 reflection seismic data (Fig. 4). Firstly, reflector terminations of geological units (e.g. sills) will
119 be much more pronounced than they will be in actual seismic data. Secondly, steeply dipping
120 interfaces will be imaged perfectly (i.e. dykes), in contrast to actual seismic which is not
121 adept at imaging steeply dipping interfaces. Thirdly, tuned reflector packages (e.g. thin sills)
122 will exhibit pronounced amplitude variations which relate to thickness-variations in 1D
123 convolution methods (e.g. Fig 4; Magee et al 2015), but these effects will be much more
124 diffuse in real seismic data, because the resolution is limited and the response from a single

125 sampled point will be influenced by adjacent points. This could lead to significant
126 misunderstandings if lessons learned from analysis of such synthetic seismic data are used to
127 guide interpretation of real seismic

128

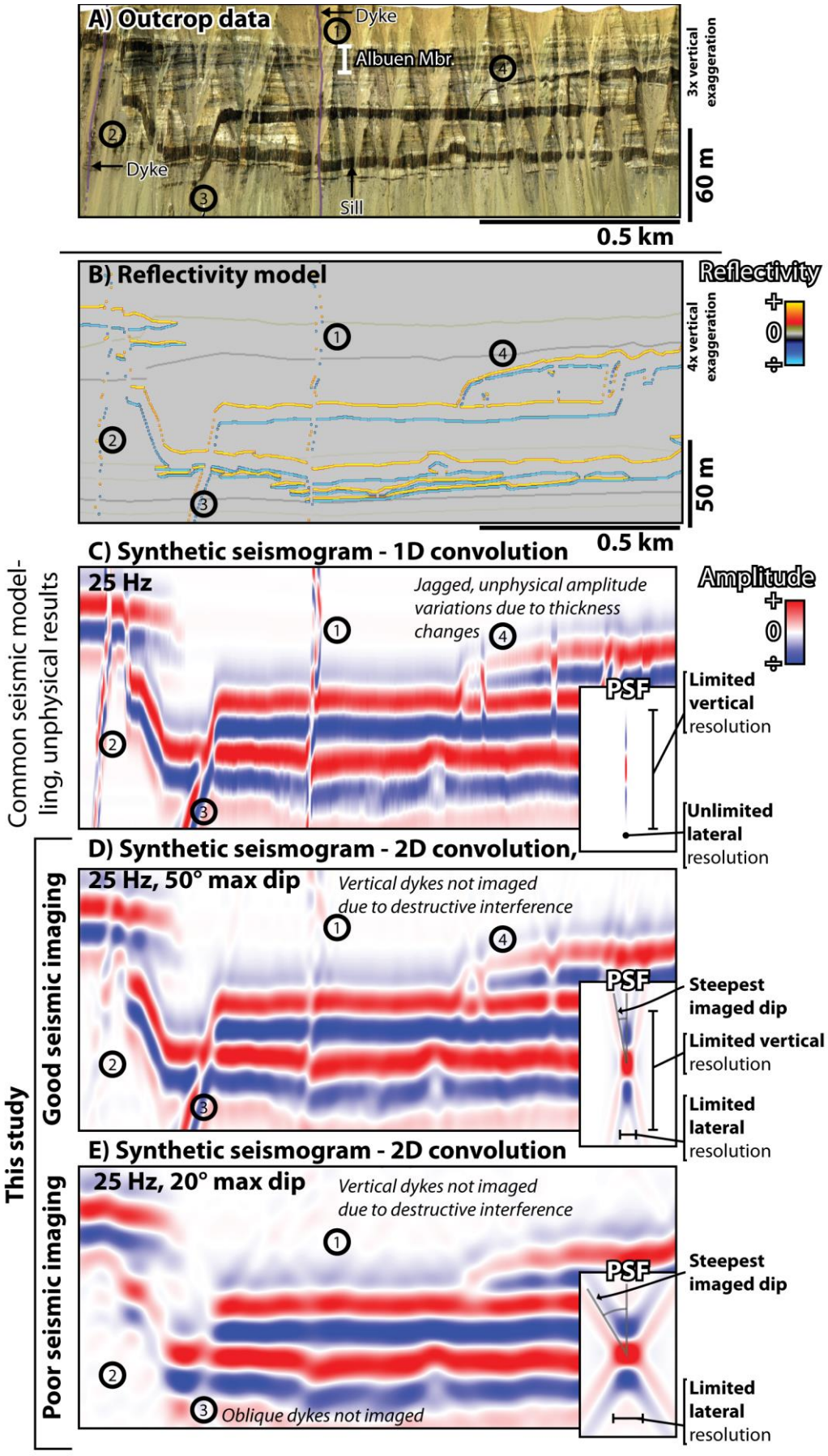
A) Outcrop data
Dyke
Albuen Mbr.
Dyke
Sill
3x vertical exaggeration
60 m
0.5 km
B) Reflectivity model
Reflectivity
4x vertical exaggeration
50 m
0.5 km
C) Synthetic seismogram - 1D convolution
25 Hz
Jagged, unphysical amplitude variations due to thickness changes
Amplitude
PSF
Limited vertical resolution
Unlimited lateral resolution
Common seismic model-ling, unphysical results
D) Synthetic seismogram - 2D convolution,
25 Hz, 50° max dip
Vertical dykes not imaged due to destructive interference
PSF
Steepest imaged dip
Limited vertical resolution
Limited lateral resolution
Good seismic imaging
This study
E) Synthetic seismogram - 2D convolution
25 Hz, 20° max dip
Vertical dykes not imaged due to destructive interference
PSF
Steepest imaged dip
Limited lateral resolution
Oblique dykes not imaged
Poor seismic imaging

Fig. 4 *(previous page): Figure illustrating the seismic convolution method, the difference between 1D and 2D convolution, and the concept of point-spread functions (PSF). A) Outcrop data from Jameson land. Intrusive rocks appear as dark bands in the cliffs. B) Reflectivity model, generated from outcrop architectures and acoustic properties from relevant wells (Table 1). C) Synthetic seismogram generated using the reflectivity model in (A) convolved with the 1D wavelet shown in the inset. Using this method, the lateral resolution is vastly overestimated and equal to the trace spacing. Dipping interfaces are shown to be imaged even though they would not be in actual seismic. D) Synthetic seismogram generated using 2D convolution and high (50°) maximum imaged dip-values. This simulates good-quality seismic with the ability to image relatively steeply dipping interfaces. E) Synthetic seismogram generated using 2D convolution and low (20°) maximum imaged dip-values. This simulates poor-quality seismic which does not have the ability to image steeply dipping interfaces. In particular, note these four main issues: (1) Near-vertical dykes are well-imaged in synthetic seismic based on 1D convolution, but are not imaged well due to destructive interference in the 2D-convolution cases. (2, 3) Steeply dipping (c. 45°, 30°) dykes are not imaged in poor-quality seismic. (4) Because adjacent traces do not influence each other in 1D convolution, the reflectors show a jagged and unphysical amplitude variation, which are not be present in the 2D convolution models.*

Shallowly emplaced (<1.5 km) intrusions, which often show saucer-shaped morphologies (Fig. 3; Hansen and Cartwright, 2006a; Galland et al., 2009), are generally well-imaged and well understood, as these often occur shallowly without overlying high-velocity layers. However, architectures of deeply emplaced (> 1.5 km) sill complexes have been subject of much fewer studies than their shallow counterparts, and their architectures thus are less understood (Schofield et al., 2012a; Eide et al., 2017). Furthermore, these are often more poorly imaged in seismic data due to a thicker overburden and overlying intrusions (Fig. 3). This leads to reflection and absorption of seismic energy and attenuation of the

155 seismic signal particularly at high frequency ranges (Fig. 3c, d; Gallagher and Dromgoole,
156 2007). Additionally, diversion and spreading of large-incidence ray paths occur, leading to
157 both lower resolution and inability to image steeply dipping features at depth.

158 These imaging issues commonly lead to intrusions which are not imaged at all,
159 intrusions that are imaged as tuned packages making thickness estimates difficult, multiple
160 intrusions imaged as a single one due to interference effects, and unimaged steeply dipping
161 features. Such effects become more pronounced with increasing depth.

162 2. Geological setting

163 The synthetic seismic generated in this study is based on architectures of igneous intrusions
164 and host rock from a field area near the SE margin of the Jameson Land Basin (Fig. 2) in East
165 Greenland (Eide et al., 2017). The host-rock was deposited in the Early-Middle Jurassic
166 during a post-rift thermal sag phase (Surlyk, 2003), and comprises a variety of shallow-marine
167 tide-influenced deposits, deposited close to the basin margin (Dam and Surlyk, 1998; Ahokas
168 et al., 2014; Eide et al., 2016). The Jameson Land Basin was a minor sub-basin in the
169 Mesozoic seaway between Norway and Greenland, and the sedimentary host rocks are
170 time- and facies equivalent to the Båt Group, which is a prolific reservoir interval on the
171 conjugate Haltenbanken area on the Norwegian Continental Shelf (Martinius et al., 2001;
172 Ichaso and Dalrymple, 2014; van Capelle et al., 2017). Late Jurassic-Cretaceous rifting and
173 Paleogene volcanism led to deposition of c. 3 km of sediment and lava flows above the study
174 interval (Brooks, 1973, 2011; Larsen and Marcussen, 1992; Mathiesen et al., 2000; Surlyk,
175 2003). Deposition of a significant overburden led to extensive quartz-cementation prior to
176 emplacement of igneous intrusions (Hald and Tegner, 2000). The detailed sill architecture
177 and emplacement of these intrusives are covered by Eide et al (2017).

178 The studied sills are part of the mafic Jameson Land Suite, and consist of nonvesicular,
179 aphyric tholeiitic dolerites with ophitic texture (Hald and Tegner, 2000), and vary in
180 thickness from c.1 – 18 m, with an average thickness of 9 m (Eide et al., 2017). The
181 architecture and morphology of the sills is clearly influenced by the host-rock lithology, as
182 they favour mudstone units, avoid well-cemented homogeneous sandstone units, and show
183 clear ductile/non-brittle emplacement features in poorly-cemented sandstone intervals (Eide
184 et al., 2017). For the purpose of this study, the intrusives and Jurassic host-rock can be
185 divided into seven facies associations (Figs. 2B, 5; Table 1): 1: Paleogene *dolerite intrusives*, 2:
186 *Homogeneous sandstone*, 3: Bedded *sandstone* with thin mudstone intervals, 4: *Poorly cemented*
187 *sandstone*, due to the presence of chlorite overgrowths (c.f. Ahokas et al., 2014), 5:
188 *Heterolithic* beds, comprising interbedded 1-50 cm thick sand- and mudstone beds with a
189 variable but overall approximately equal proportion of sandstone and mudstone, 6:
190 Regionally extensive *mudstone* intervals, and 7: *organic rich mudstone* intervals (c.f. Krabbe et
191 al.,1994).

192

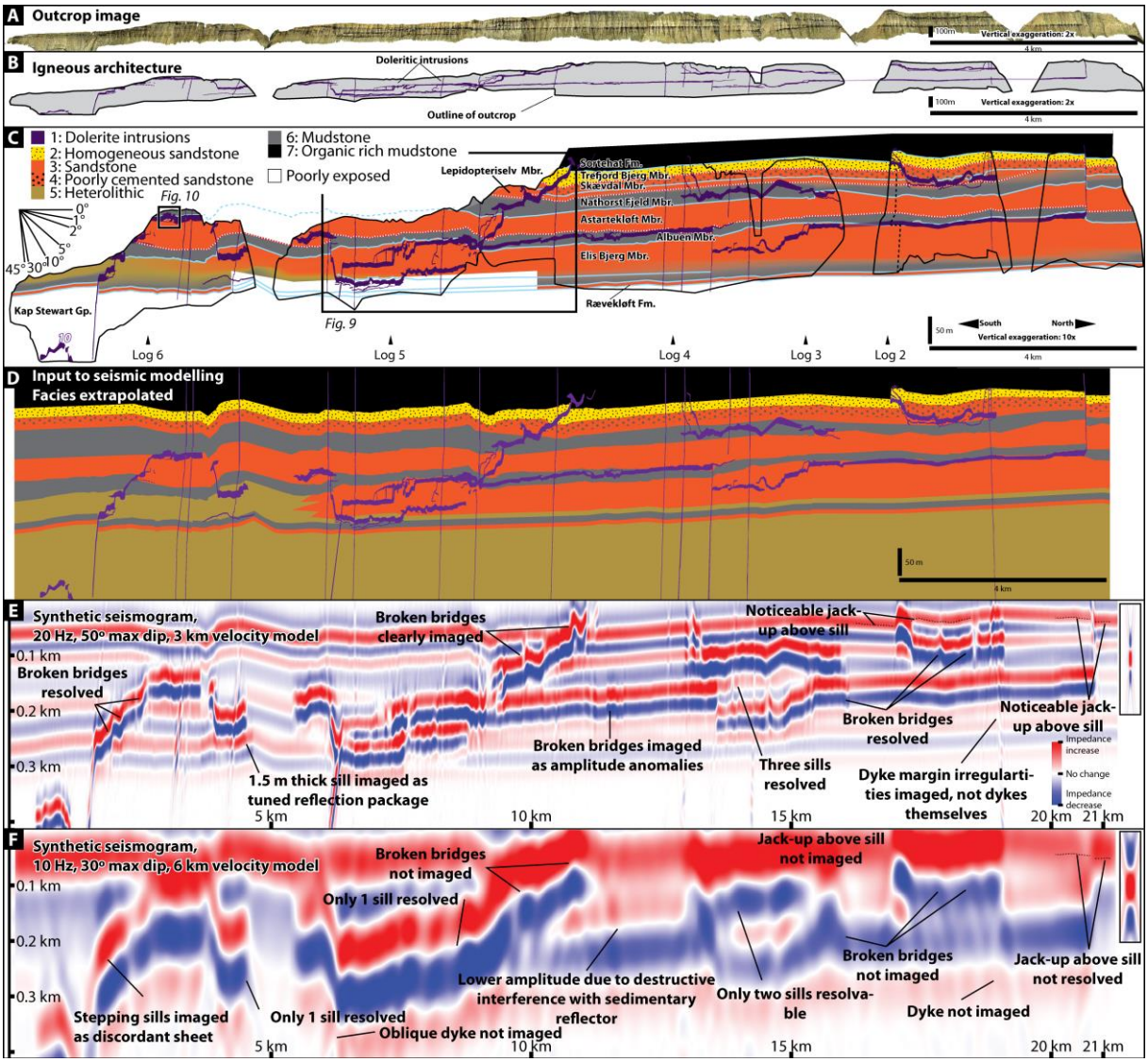

Fig. 5: *Outcrop data and synthetic seismograms. For location, see Figs 1, 2. A) Studied outcrop. B) Igneous architecture from outcrop. C) Stratigraphic and igneous architecture. Note the tendency for intrusions to follow mudstone units, the consistent upwards-stepping of intrusions in other lithologies than mudstone, and the jack-up of host-rock above sills. D) Input model to seismic modelling, populated with acoustic properties from Table 1. E) Synthetic seismogram corresponding to model A in Fig. 7. F) Synthetic seismogram corresponding to model C in Fig. 7.*

The sills in Jameson Land are examples of a small-volume (c. 10% of studied outcrop sections) sill complex intruded deeply (3 km) into what was mainly brittle, layered host rock at the time of emplacement, which has subsequently been uplifted (Mathiesen et al., 2000;

Eide et al., 2017). This is in contrast to many exposed examples of sill complexes around the world. For example, the sills in the Karoo Basin of South Africa are associated with somewhat larger intrusion volumes, and were emplaced at shallower levels, where the host rock was likely not well consolidated (Schofield et al., 2010; Svensen et al., 2015). Other relatively well-studied examples, such as the sills emplaced in the Theron and Transantarctic Mountains of Antarctica were emplaced at a similar depth and in similar lithologies, but are the results of much higher intrusion volumes as these attain thicknesses of up to 330 m (Hersum et al., 2007; Jerram et al., 2010). The architecture and depth of intrusion the Jameson Lands Suite makes it broadly comparable to intrusions seen at deep levels (~ 3-4 km), around the Base Cretaceous/Top Jurassic, in the present day contemporaneous basin fill along the NE Atlantic Margin (c.f. Schofield et al., 2015).

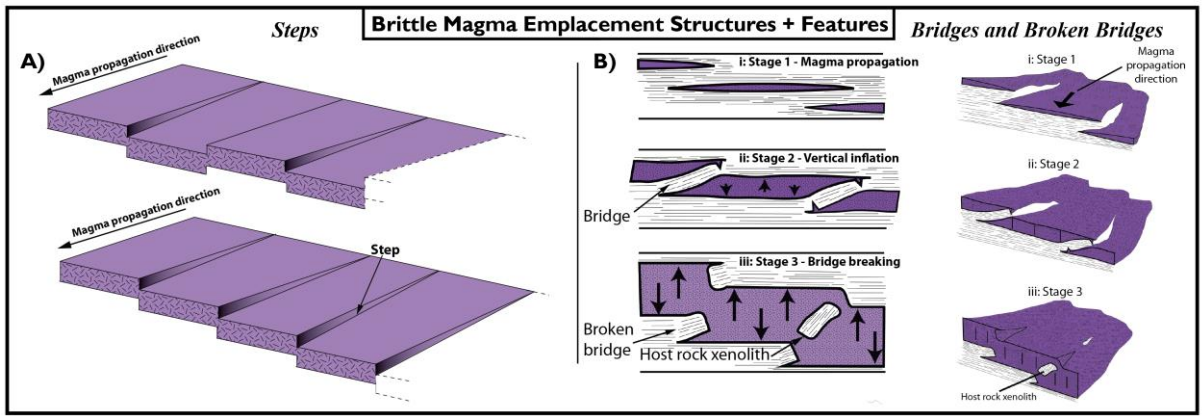

Fig. 6: *Overview of sill structures and features formed during emplacement and progressive inflation of sill intrusions in brittle host rock. A) Expression of steps on sill margins and how they relate to the magma propagation direction. B) Development of broken bridges through vertical inflation of sills and breaking of host-rock bridges between sill segments. Modified from Schofield et al. (2012a).*

3. Sill architecture in studied outcrop section

The sedimentary and igneous architecture of the studied outcrop in Jameson Land is shown in Fig. 5. A variety of features noteworthy for the present study occur in this section, and these are summarized from Eide et al. (2017): Individual sills are broadly layer-parallel and constitute c. 10% of the material in the outcrop section. *Main sills* make up 70% of the intruded volume, and these are 7-12 m thick, with average thickness of 9 m. These are associated with *sill splays* which are less than 2 m thick minor sills which occur close to the main sills where the sills are propagating in other lithologies than thicker mudstone interval.

The type of host rock (*mudstone*, *brittle interbedded sandstone and mudstone*, *brittle homogeneous sandstone*, and poorly cemented sandstone) is a major controlling factor on the architecture of sills. The majority of sills (c. 60%) are emplaced within mudstones (FA6), and sills show great vertical stability and attain lengths of up to 6 km when emplaced in regional mudstones. Sills emplaced in well-cemented interbedded sandstone (FA 2) and mudstone (FA 5) make up c. 25% of sill volume, and show abundant *broken bridge*-structures (Fig. 6) and cross-cut stratigraphy and propagate towards regional mudstones (Fig. 5C). Broken bridge structures form as two vertically offset sills inflate, bend the host rock "bridge" formed between them, which and finally break and are filled with magma (Hutton, 2009; Fig. 6). These are important indicators for magma propagation directions (Schofield et al., 2012a), and unbroken bridges may form pathways for hydrocarbon migration. Sills in other lithologies constitute a minority (15%) of the intrusive material in the outcrop, but show complex splaying geometries in homogeneous sandstones (FA2), and both ductile and brittle emplacement features in poorly cemented sandstones (FA4).

E-W-trending, near-vertical (dip > 80°) dykes occur in the study area (Figs. 2A; 5C), and these vary from 1-10 m wide, and only a small number of these are interpreted to postdate

the main intrusive phase based on cross cutting relationships, the rest are believed to be coeval with the dykes as radiometric ages are coherent and cross-cutting relationships are not observed in these (Hald and Tegner, 2000). Together, sills and dykes compartmentalize the host rock into intrusive-bounded blocks c. 0.2-4 km wide and 20-120 m thick.

Intrusion of c. 10% of igneous material into the outcrop volume appears to be solely accommodated by 1:1 uplift of host-rock above sills, as no deformation of the rock apart from sill intrusion is observed. This is proven as stratigraphy restores without error by removing the sills from images taken orthogonal to the plunge of the beds (Eide et al., 2017, their fig. 10). This indicates that deeply emplaced sills (> c. 1.5. km) formed as fractures which inflated vertically in a piston-like fashion.

The sum of these observations show that sill complexes have complicated architectures and that details of the architecture might have significant implications for sill emplacement, reservoirs and hydrocarbon systems (c.f. Rateau et al. 2013; Senger et al., 2017). How these details are imaged in seismic data will be studied in the remainder of this contribution.

4. Methods and dataset

4.1 Outcrop data

The synthetic seismic models are based on analysis of the Jameson Land Suite mafic sill complex and surrounding host-rock of the Neill Klinter Group, imaged in a 22 km long and 250 m high virtual outcrop model (Figs. 2A, 5A) acquired using oblique helicopter-mounted LIDAR-scanning. The outcrop model was acquired using the Helimap System (Vallet and Skaloud, 2004), using a laser scanner, a digital medium format camera with a 35 mm lens, and an inertial navigation system. Processing of these data (see Buckley et al., 2008; Rittersbacher et al., 2014; Eide et al., 2016) yielded a high-quality virtual outcrop model devoid of errors

266 with 0.3 m point spacing and a pixel resolution of c. 7 cm. The outcrop model is constrained
267 by a set of six sedimentary logs with a total thickness of 1040 m, acquired along the outcrop
268 with the objective to sample the entire section. The outcrop is oriented north-south, and
269 yields a strike-section through the sedimentary systems (Dam and Surlyk, 1998). Apart from
270 a general proximal-to-distal trend leading to more fine grained deposits southwards in the
271 outcrop throughout all stratigraphic units, the lateral lithological variability is low (Dam and
272 Surlyk, 1998; Eide et al., 2016), leading to a good constraint on lithology, and ultimately
273 petrophysical properties used for modelling, in the entire dataset. The outcrops are
274 generally unfaulted, tectonic dip is on average 3° towards the west, and the sills are generally
275 parallel to sedimentary layering.

276 ### 4.2 Synthetic seismic modelling

277 The synthetic seismic models of the studied section yields data that simulate zero-phase,
278 pre-stack depth-migrated (PSDM) reflection seismic data (Lecomte et al., 2015). The
279 methodology applied for modelling is based on ray-tracing modelling for study of the
280 overburden effects (Gjøystdal et al., 2007; Fig. 7), and on 2D convolution (Fig. 4) for the
281 generation of synthetic seismic models of the target interval (c.f. Lecomte et al., 2016).
282 Detailed reviews of these methods are out of scope of this paper and therefore only briefly
283 summarised here.

284 Four main parameters are critical for the seismic modelling presented in this study: rock P-
285 wave velocity, rock density, seismic frequency at the target depth, and maximum imageable
286 dip (*max dip*) at the target depth. In reality, these parameters vary with the depth of the
287 modelling target, the geological history of the target and overburden, and the overburden
288 architecture. P-wave-velocity and density of host-rock and overburden are taken from
289 relevant depths in time-equivalent formations on the Norwegian Continental Shelf (Table 1),

and P-wave-velocity and density for igneous intrusions is from Smallwood and Maresh (2002). Seismic frequency at the target depth is measured from a publically available 3D seismic dataset from the Møre Basin (NH003, "*Solsikke*") in the base case, and from the BG0804-survey in the Barents Sea in the case of an eroded basin (Fig. 8). It is worth pointing out that vertical resolution in seismic data is a function of the signal frequency and host rock velocity, while the lateral resolution is a function of signal frequency, host-rock velocity and max dip (c.f. Figs 4d, e). In each modelled scenario, the lateral resolution has been ascertained using ray-tracing methods (Fig. 6) to investigate the max dip and investigation of seismic frequency in comparable datasets to investigate the seismic frequency (Fig. 7).

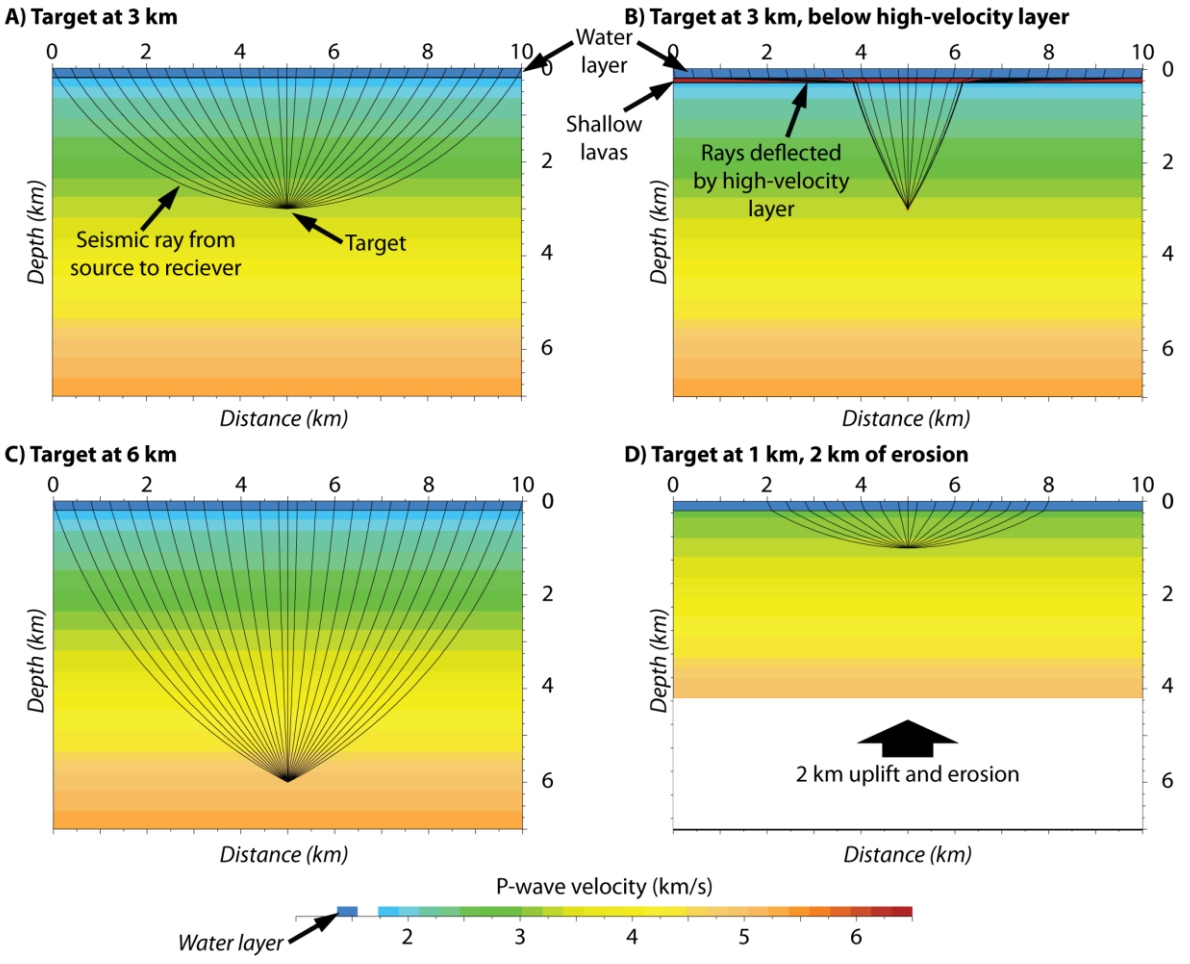

Fig. 7: *Overburden models, generated to investigate ray propagation and resulting lateral resolution for each of the modelling cases. Interfaces hit by rays with a large variety of incidence angles will*

have high lateral resolution, and more steeply dipping interfaces are imaged. A) Model with linear P-wave velocity gradient based on well data from the Norwegian Continental Shelf. B) Model with a linear P-wave velocity gradient and an overlying high-velocity layer (i.e. shallow intrusions, lavas). Note the steep incidence of rays reaching the target, resulting in low lateral resolution. C) Model with linear P-wave velocity gradient and target at 6 km. Note the steeper incidence of rays compared with (A). D) Model with the upper 2 km of stratigraphy eroded, resulting in a hard sea-floor. Note the large variety of incoming angles.

Interpretations of sedimentary units and intrusions on the virtual outcrops from Jameson Land yielded scaled, georeferenced lines which have been projected onto a plane parallel to the outcrop and orthogonal to the plunge of the tectonic dip of layers. As the lateral lithological variability is quite low (Eide et al., 2016), extrapolation of stratigraphy and sill architecture into unexposed areas was straightforward (Fig. 5D).

The seismic modelling procedure utilized in this paper consists of the following steps: (1) Four different conceptual overburden models are created using specified layer interfaces, velocity gradients and petrophysical properties derived from relevant wells from the Norwegian Continental Shelf (Fig. 7, Table 1). (2) Wave-propagation from seismic source, through the overburden model, to the target depth, and then back to receivers is simulated based on ray-based algorithms in order to investigate max dip, which is used to define a two-dimensional spatial "wavelet" (termed Point-Spread Function (PSF), c.f. Fig. 4) based on dominant frequency of the signal at depth of interest. (3) Creation of a target reflectivity model using layer architectures obtained from outcrop analysis (Fig. 5D) and petrophysical properties from appropriate subsurface analogues in wells (Table 1). (4) 2D convolution of the target reflectivity model with the PSF obtained in Step 2.

4.3 Overburden models

This section contains an overview of imaging parameters (max dip and dominant frequency) based on the four overburden scenarios presented in Fig. 7). All models are constructed with a 0.2 km thick water layer, and a linear P-wave-velocity gradient from 1.8 km/s at the seabed, 3.3 km/s at 3 km, and 4.8 km/s at 6 km.

Model A (simple overburden) investigates a base-case, where the target intrusions are simply overlain by 3 km of sedimentary host rock (Fig. 7A).

Model B (overlying igneous rocks) investigates the influence of an overlying high-velocity layer, here modelled as a 100 m layer of basalt at the seabed (Fig. 7B). Several other geometries of overlying high-velocity layers have also been modelled, and gave similar results.

Model C (deep burial) tests the effects of further burial of the target interval to 6 km (Fig. 7C), resulting in increased host-rock velocity at the target interval (Table 1b).

Model D (uplifted and eroded basin) tests the effect of 2 km of erosion of the overburden (Fig. 7D), yielding a P-wave velocity of 2.9 km/s at the seabed and a target at 1 km depth where the average seismic velocity is 3.3 km/s.

4.3.1 Seismic frequency

Frequency attenuation with depth is difficult to model well, and signal frequency versus depth is therefore taken from the *Solsikke* 3D seismic survey from the Møre Basin (Fig. 1) for models without erosion (Fig. 7A-C). Shallow sills, presently at c. 1 km below the seabed, are imaged at c. 40 Hz. Deeper intrusions at c. 3 km below the seabed, are imaged at c. 18 Hz, which is similar to what is observed in other localities on the N Atlantic Margin, such as in the Faroe-Shetland Basin (Schofield et al. 2015), where the sills occur at relatively deep levels within the contemporaneous basin fill. Significant attenuation of high frequencies (>25 Hz) occur just below shallow sills (c.f. Fig. 3). At depths of c. 3 km in areas underlying shallow sills, the dominant frequency is c. 13Hz, a significant reduction compared to 18 Hz in areas without overlying sill intrusions (Fig. 8B). For model D, where 2 km of overburden has been eroded, frequency versus depth has been taken from the BG0804-survey in the Barents Sea (Fig. 1) where the depth of erosion is similar (Henriksen et al., 2011; Baig et al., 2016), and a number of exploration wells provide excellent depth control. At c. 1 km depth, the dominant frequency is 40 Hz (Fig. 8B).

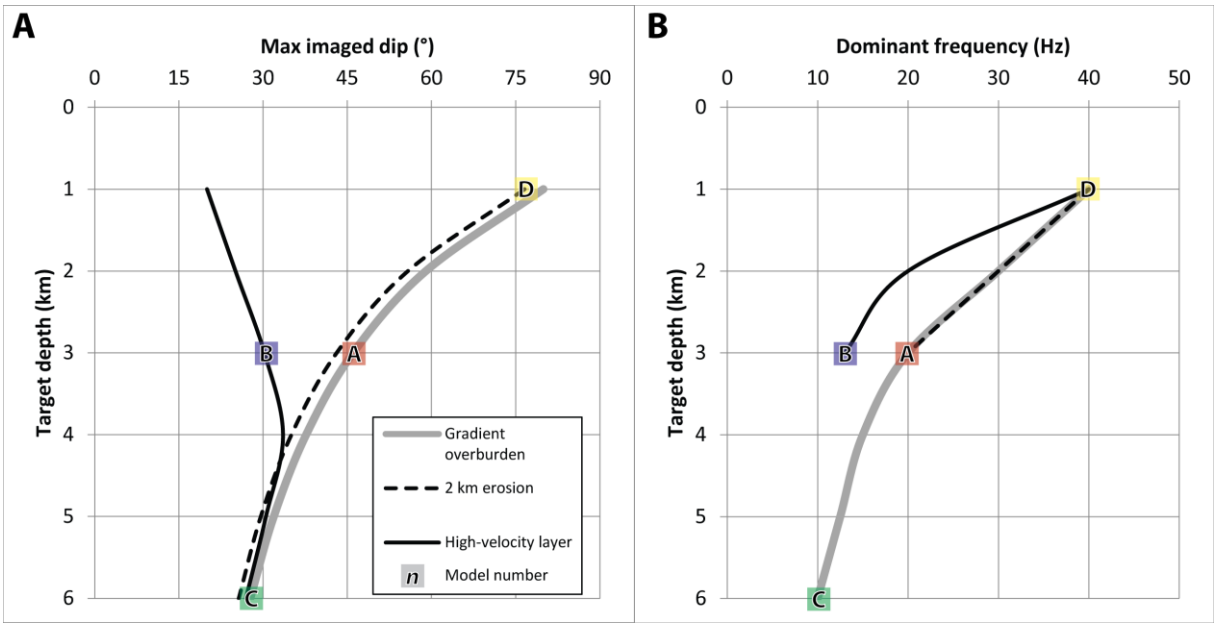

Fig. 8: Imaging properties used for seismic modelling. Inset letters show properties at target depth corresponding to cases in Fig 7. A) Max imaged dip calculated from models in Fig. 7. B) Dominant frequency at depth, derived from analysis of 3D seismic datasets.

4.3.2 Illumination and overburden effects

The main goal of the overburden modelling is to investigate the max dip and thus also the lateral resolution which can be expected to occur in different cases and at different depths. Using a ray-tracing approach, lateral resolution in seismic data is a function of the max dip, and this is illustrated in Fig. 4. The modelling shows that the models can be grouped into three groups which behave similarly (Fig. 7):

Models with a simple overburden (Fig. 7A,C) have high max dip (and hence high lateral resolution) at shallow depths (c. 80° at 1 km), and decrease rapidly to c. 45° at 3 km and 30 ° at 6 km.

In the models with high-velocitiy layers above the target, only rays with steep incidence angles may reach the target, as lower-incidence angle rays are refracted away from the target (Fig. 7b). This leads to a significant reduction in max dip, to c. 30° at 3 km depth (Fig. 8A)

In the models with 2 km erosion, the maximum imageable dip is close to, but slightly higher than models with a simple velocity-gradient in the overburden (Fig. 7A). The strong velocity

contrast at the seabed caused by a hard sea-floor will increase the potential for strong multiples. This would lead to potentially worse imaging than is accounted for here, and costlier processing.

4.3.3 Summary of overburden effects

In summary, the modelling of overburden effects and inspection of publically available 3D-seismic data from relevant basins indicate that for models with a simple gradient overburden, seismic frequency and max dip decrease gradually with depth (Fig. 7). For models with overlying high-velocity layers such as lavas and/or shallow intrusions, a sharp decrease in max dip and high-frequency content occurs once the seismic waves hit the high-velocity layers. This leads to poorer imaging of underlying features such as sill complexes. The eroded models show a moderate worsening in lateral resolution, and a frequency-loss with depth comparable to models with simple gradient.

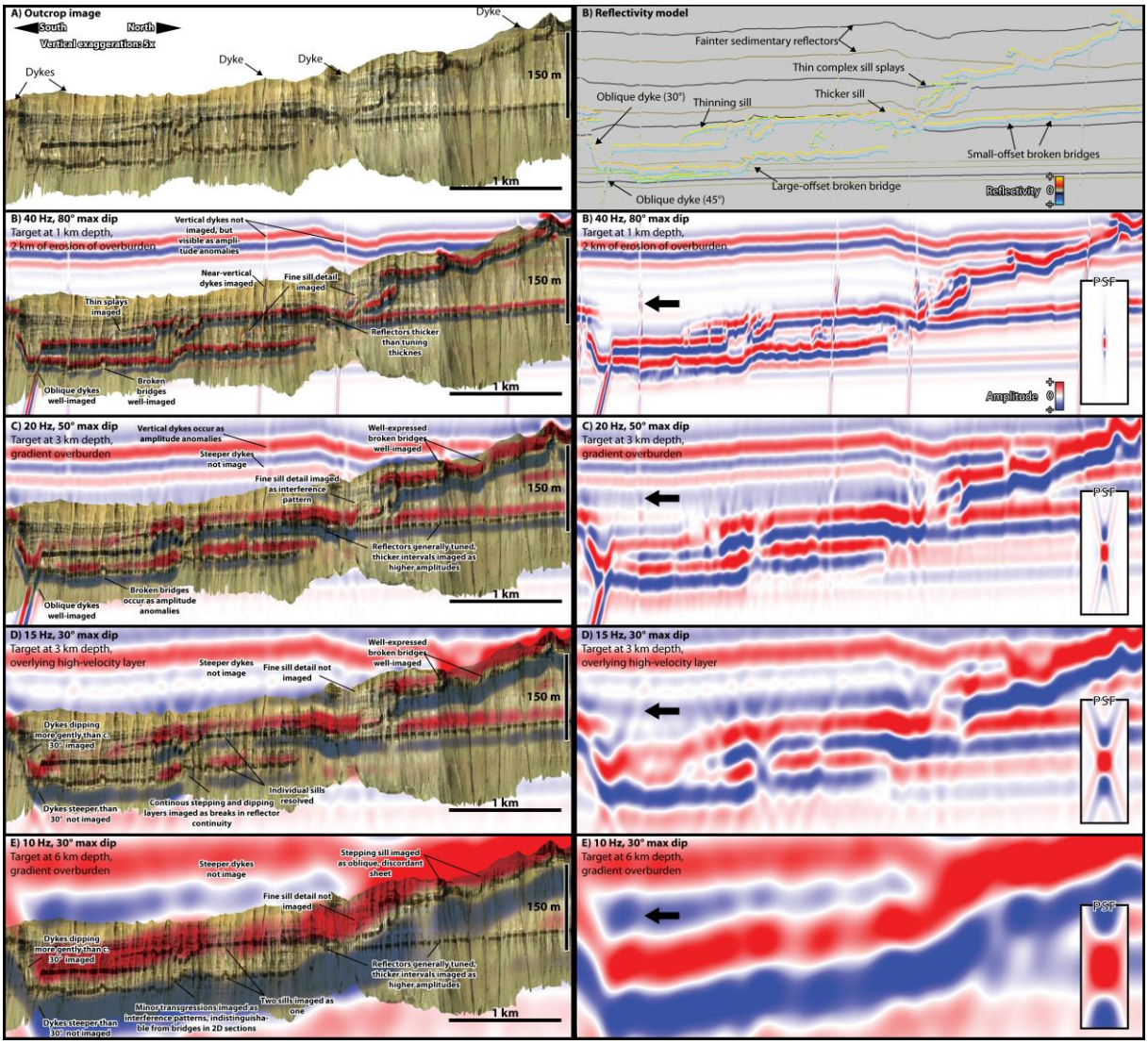

389

390 **Fig. 9:** Comparison of details of synthetic seismograms. See Fig. 5C for location. A)
391 Outcrop image and reflectivy model. B) Synthetic seismogram corresponding to model D in
392 Fig. 7. C) Synthetic seismogram corresponding to model A in Fig. 7. D) Synthetic seismogram
393 corresponding to model D in Fig. 7. E) Synthetic seismogram corresponding to model C in
394 Fig. 7. Note that this model is generated using velocity model B in Table 1.

5. Forward seismic modelling

5.1 Base case: target at 3 km depth, simple overburden

For an overburden model with a linear velocity gradient, a target at 3 km depth, and an average host-rock P-wave velocity of 3.1 km /s at the target, the modelling indicates that high-quality, depth-migrated, zero-offset seismic data will appear similar to Fig. 5E. Despite the modest thickness of main sills (7-16 m) and relatively low seismic frequency (20 Hz) the sills are still clearly imaged in the synthetic seismogram, with reflections from the intrusions showing much higher amplitudes than reflections from sedimentary interfaces. Tuning thickness (e.g. Brown, 2011) is commonly taken as a quarter wavelength, which in this case (V_P=3.1 km/s, f=20 Hz) is c. 40 m. The sills are still visible, despite being thinner than seismic resolution, due to the large impedance contrast between host-rock and intrusions (c.f. Table 1a). Even sills as thin as 1.5 m are resolvable as amplitude anomalies, but it is likely that these could not be resolved in actual seismic data due to presence of noise.

The architecture of the sill complex is generally well-constrained in the synthetic seismogram, and both sills and oblique dykes with dips shallower than 45° are imaged. Broken bridges (c.f. Fig. 6) with large offsets (> 15 m) are clearly imaged as large steps in the simulated reflections, while broken bridges with offsets smaller than 15 are imaged as local amplitude anomalies in otherwise continuous reflections (Fig. 9C, 10c). It is likely that these amplitude anomalies caused by small-offset (< 15 m) broken bridges could not be separated from seismic noise in real seismic data. The steps observed on the investigated sill margins are not detectable in the seismograms, and this is probably due to the small step heights in this dataset, which are 2 m on average. In this seismogram, the broken bridges would be indistinguishable from larger-offset steps. Each sill in this data is generally imaged separately, as they are spaced more widely than ½ seismic wavelength.

Steeply dipping to vertical igneous features (> 50°) i.e. dykes, are not imaged directly in this seismogram, but dykes are still resolvable in the seismogram (Fig. 9C). This is mainly due to two reasons: (1) dyke margin irregularities are imaged instead of the dykes themselves, and (2) dykes lead to disruptions in original layer continuity that leads to discontinuities in the seismic data that may be interpreted as dykes. In simulations with lower lateral resolution, this is not imaged (Figs 9D,E).

Pronounced jack-up of host-rock above sills is common in the dataset from Jameson Land Greenland (Eide et al., 2017). This is resolvable in the synthetic seismogram, particularly near the top at 17 and 21 km (Fig. 5E), where the reflections from the sedimentary bedding are clearly offset across dykes and transgressive sills.

In a close-up view (Fig. 9C), m-scale sill splays are imaged as complex interference patterns.

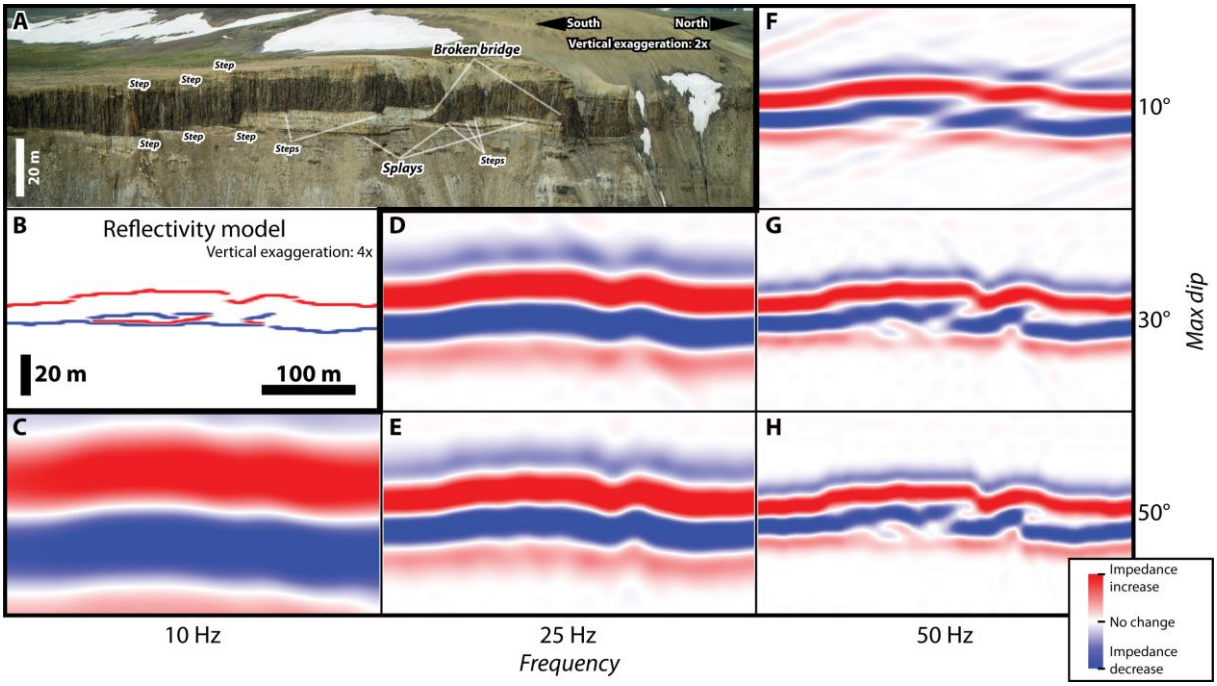

Fig. 10: *Seismic imaging of broken bridges, steps and sill splays. See Fig. 5C for location. A) Outcrop image showing abundant splays, steps and broken bridges. B) reflectivity model generated from (A). C-H) Synthetic seismograms showing imaging with different lateral resolution (expressed as max imageable dip) and dominant frequency. Note especially the influence of a decrease in lateral resolution (F, G and H).*

5.2 Deep target: target at 6 km depth, simple overburden

For a target at 6 km depth, increased seismic velocity and density due to increasing compaction and diagenesis must be taken into account (Table 1b). For an overburden model with a linear velocity gradient, a target at 6 km depth, and an average host-rock P-wave velocity of 4.5 km /s, the modelling indicates that high-quality, depth-migrated, zero-offset seismic data will appear like in Fig. 5F. In this case, the dominant frequency would be 10Hz, yielding a tuning thickness of c. 100 m. Individual main sills (7-16 m thick) are not imaged, but

instead the entire sill-complex appears as one single, complex reflector, and shows the highest amplitudes of all reflections in this seismogram due to the large amplitude contrast between intrusives and host-rock. However, at such depths, the amplitude contrast between host-rock and intrusives are smaller, and significant local amplitude decreases due to destructive interference occur. This happens particularly between dolerite intrusions and the overlying reflection generated at the interface between the Astartekløft Member and Nathorst Fjeld Member, for example at 12 km (Fig. 5F).

Prominent stepping sills, such as at 2 and 9 km along the profile (Fig. 5F), are imaged as oblique sheets which are discordant to bedding. Broken bridges are in some instances imaged as amplitude anomalies, but these are generally indistinguishable from amplitude anomalies generated by interference with reflections from host-rock stratigraphy. Due to loss of lateral resolution at depth, oblique dykes dipping more than c. 30° are not imaged due to destructive interference (Figs. 5F at 7 km; 9E).

In several cases, such as at 7 km along Fig. 5F, closely spaced sills only generate one compound reflection, and individual sills are therefore not resolvable. Jack-up of host-rock above sills at the scale observed in this outcrop (c. 8 m) is not resolved (Fig. 5F).

5.3 Imaging below high-velocity layers

Reduction in both the seismic frequency and lateral resolution below shallow sills is evident from analysis of the studied seismic data and overburden modelling (Figs 3, 7). This leads to a prominent decrease in seismic quality (c.f. Figs 9C,D), which is particularly evident in the broadening and thickening of the point-spread-functions (c.f. insets in Figs 9C,D). In the generated seismograms, the effect of decreasing the lateral resolution, and thereby the ability to image more steeply dipping interfaces, is striking. Broken bridges are not well imaged anymore, and stepping sills rather occur as oblique sheets. Steeply dipping oblique dykes (>35°) are not imaged, and amplitude anomalies related to presence of vertical dykes are no longer modelled to occur because of the low lateral resolution. Furthermore, decreased frequency leads to less well-defined reflectors. Imaging of fine-scale features with varying frequency and lateral resolution is covered comprehensively in Fig. 10.

5.4 Shallow imaging

Provided that seismic acquisition-problems related to hard seafloor can be overcome, the model with 2 km of erosion (Fig. 7D) resulted in the best quality seismic (Figs. 9B,). In

particular, compare the point-spread-function of this seismogram to the others (inset in Fig. 9B). In this case, the synthetic seismogram shows a remarkable similarity to the input model, due to the high frequency and the high max dip, yielding high lateral and vertical resolution. Tuning thickness (19 m) is close to the sill thickness, and a clear relationship between thinning of sills and decrease in amplitude occurs. Steeply dipping interfaces, broken bridges and steps are clearly imaged, and even some meter-scale sill-splays are resolved.

6. Discussion

6.1 Seismic resolution and seismic detectability of igneous sills

6.1.1. Seismic Resolution and Amplitude of Igneous Intrusions

In order to understand issues with imaging igneous sill complexes in reflection seismic data, seismic resolution and seismic detectability must be discussed. The limited range of frequencies available in seismic surveys leads to limitations in the lower limit of bed thicknesses that may be uniquely resolved (e.g. Simm and Bacon, 2014). The limit of thickness of beds that may be resolved is termed vertical resolution, and the seismic resolution is commonly approximated to be ¼ of the dominant wavelength ($\lambda = v_p / f$) of the signal, however, the exact value is dependent on the wavelet shape (e.g. Simm and Bacon, 2014). This is illustrated in Fig. 11, where imaging of a 100 m thinning wedge is simulated using a 2D point-spread function (PSF). Using a PSF based on a Ricker wavelet, onset of tuning occurs at λ/3 (c. 45 m). At wedge thicknesses greater than 45 m both the top and the bottom of the wedge is imaged as separate reflectors. The bed is therefore not resolved at thicknesses smaller than c. λ/3.

As the bed thickness approaches λ/4 (35 m), the side-lobes of the lower reflection start to interfere constructively with the main lobe of the upper reflection, leading to increased amplitude in this thickness range. At wedge thicknesses lower than c. λ/3, the thickness of the wedge may not be determined from the reflected signal, and his is known as the *tuning effect, tuning thickness* or the *Rayleigh Criterion* (e.g. Kallweit and Wood, 1982). The distance between the maximum amplitudes of the upper and lower reflector does thus not change as the wedge thins past the tuning thickness in Fig. 11D. As the main lobe of the upper reflection interferes constructively with the side-lobes of the underlying reflection, the

reflection amplitude increases to a peak of c. 1.4x the normal amplitude. Peak tuning occurs at c. λ/5 (28 m).

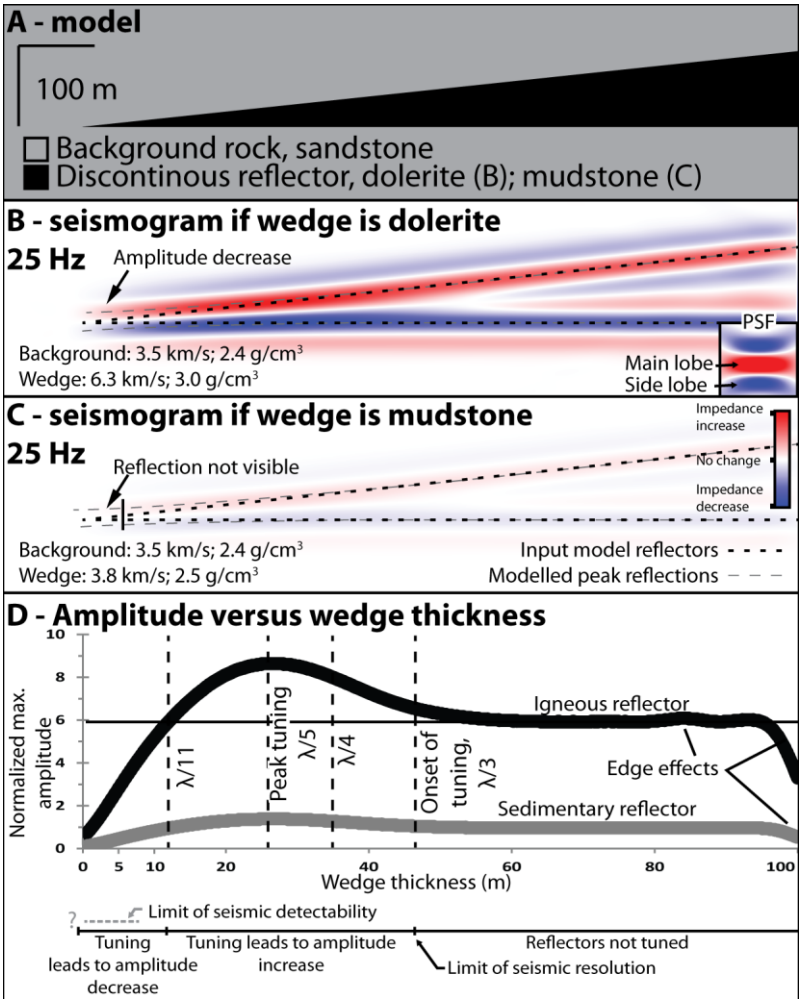

Fig. 11: Wedge-model illustrating the concepts of seismic tuning, seismic resolution and seismic detectability. Wavelength (λ) = 140, λ /4 = 37.5 m. A) Input model geometry. The model is 1 km long, and contains a 900 m long wedge thinning towards the left from 100 to 0 m. B) Resulting seismogram at 25 Hz using the inset PSF for a wedge consisting of dolerite within sandstone. Note the clearly resolved top and basal reflectors for wedge thicknesses from 100-45 m, the increased amplitude and overestimated thickness due to seismic tuning from 45-12 m wedge thickness, and the rapid amplitude decrease for wedge thicknesses of 12-0 m. C) B) Resulting seismogram at same conditions and amplitude scale for a mudstone wedge within a sandstone. Note the decreased amplitude compared to (B), and the lack of visible reflections at wedge thicknesses smaller than c. 10 m. D) Graphs showing normalized maximum amplitude per trace for (B) and (C). Note the similarity in the seismic signal for intrusions which are c 40 m thick and c. 10m thick, indicating that relatively thin intrusions such as the ones in this study would be nearly indistinguishable from thicker intrusions in seismic data as long as the intrusions are thinner than seismic resolution.

As the wedge thins further than the peak tuning thickness of λ/5, there is an overall decrease in the amplitude strength, first because the side-lobe and main lobes interfere in a non-optimal way, and then as the oppositely-directed upper and lower main lobes starts to interfere with each other. In the modelling run presented in Fig. 11, there is a gradual decrease of amplitude strength as the wedge thins further. It is important to note that the reflection amplitude at λ/11 (11 m) is equal to the reflection amplitude at the top of a dolerite reflector which is not tuned and therefore, theoretically, relatively thin intrusions should be imaged.

6.1.2 Seismic detectability of sill intrusions

The seismic detectability of an interface relates to whether a reflection from an interface can be recognized in seismic data or not. This is a much more difficult issue to address than seismic resolution, as it is a function of many more variables than the seismic resolution, some of which are poorly constrained and difficult to model. In order to detect a reflection, it needs to have a significantly higher amplitude than the baseline set by seismic noise in a survey. As seismic data is subject to significant amounts of processing to remove noise, it is hard to provide definitive answers without knowing each particular case, but we can offer some general considerations.

The amplitude of a reflection depends on the contrast in acoustic impedance (P-wave velocity × density) across the layer interface. It follows from the input values used in this study (Table 1), that doleritic intrusions have much higher P-wave velocity and density than their sedimentary host rocks. Thus, the amplitudes from the top of igneous intrusions are much higher than amplitudes from sedimentary reflectors. This is shown in Fig 11, where the amplitude of a reflector from a sandstone-dolerite interface is about 6 times higher than the amplitude of a sedimentary reflector, all other things being equal.

Assuming that the data quality of a seismic survey is good enough to image a siliciclastic sedimentary reflector at depth, it follows from the wedge model in Fig. 11D that it should be theoretically possible to image and detect reflections even from very thin dolerites (i.e. thicknesses down to a few meters). Furthermore, it also follows that sills with a thickness in the order of λ/11 (11m) would be imaged with the same reflection strength as an un-tuned reflection from a sediment-dolerite interface (Fig 11D). This implies that igneous intrusions with thicknesses as the ones seen in studied cliffs in East Greenland should be easy to detect in seismic. This is supported by Sheriff and Geldart (1995) who suggested that low-amplitude

hydrocarbon-bearing sandstone within mudstones could be detected in "reasonable data quality" at thicknesses of λ/20 – λ/30. Because these *rules-of-thumb* are determined with reflections from siliciclastic reflections in mind, and because of the much greater acoustic impedance contrast between dolerite and siliciclastic rocks, we suggest that a limit of detectability of λ/30 is probably too pessimistic *in principle* for what can be detected in good-quality seismic data. However, in reality, combined seismic and well-log datasets from areas with igneous intrusions commonly reveal large amounts of un-imaged sill intrusions (Fig. 12). In the following sections, we investigate this.

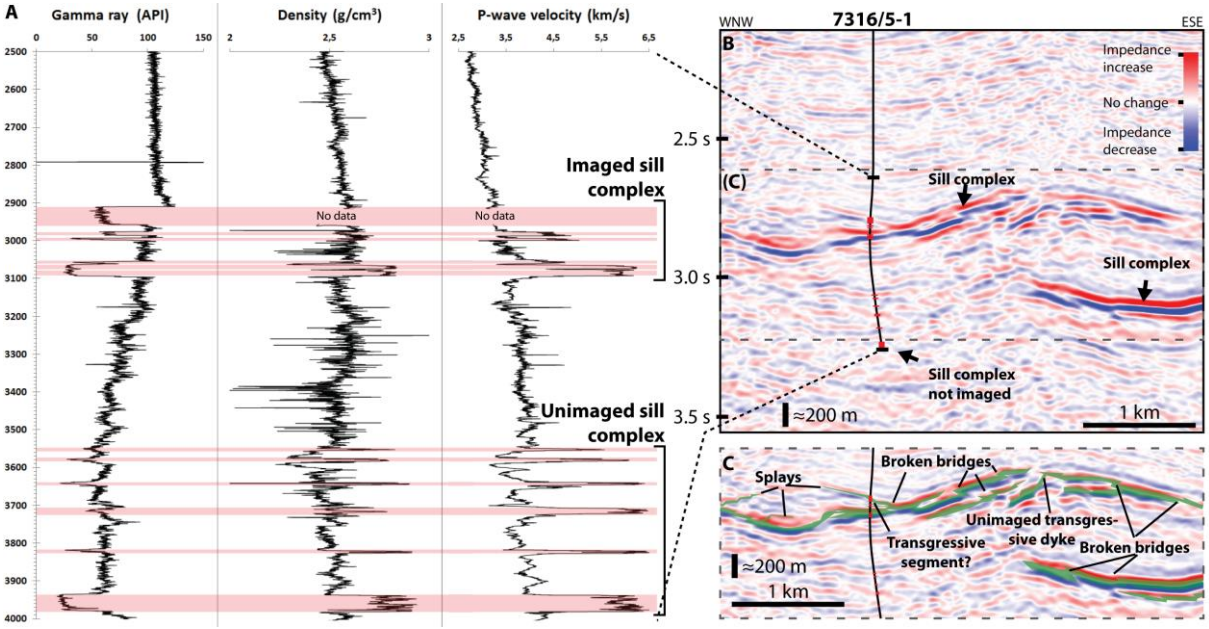

***Fig 12**: Comparison of well and seismic data of sill complexes. A) Data from well 7316/5-1 from the Vestbakken Volcanic Province on the W Barents Sea Margin. Red fields show depths of interpreted igneous intrusions. B) Uninterpreted seismic section around the well in (A). Note that only the upper sill-complex is imaged, although the lower sill complex is of similar thickness . Red fields on well indicate intrusions in (A). C) Interpreted section from B. Note the similarity of the actual seismic data to the synthetic seismograms generated from outcrop data from E Greenland, and that geometries on seismic reflectors corresponds to geometries observed in outcrop.*

6.2 Modelling limitations and seismic noise - When can we not see deep intrusions at all?

In all types of modelling, there are limitations and simplifications. The method applied here has significant advantages compared to methods used for modelling igneous intrusions in previous studies (e.g. Magee et al 2015), particularly because this model takes limitations in

horizontal resolution into account, because it includes the effect of overburden on seismic imaging at the target, and because it more accurately represents steeply dipping features such as dykes. The method applied in this study also has three particular limitations (which would also be present in 1D convolution) that should be pointed out before inferences made from analysis of the synthetic seismograms are applied to actual seismic data.

6.2.1 Dykes and near-vertical interfaces

Near-vertical (> 70°) interfaces such as steeply dipping dykes are modelled as a series of vertically offset points rather than continuous reflectors (Fig 4B). This is because reflection coefficients are calculated vertically in a grid. Furthermore, the theoretical background of ray-based seismic imaging and processing assumes relatively flat layers. However, the dykes modelled in this study (e.g. Fig 5E) resemble interpreted dykes in seismic data from the NE Barents Sea (Minakov et al., 2017, their fig. 5), showing that the representation of dykes in the model achieves acceptable results.

Interestingly, in seismic data with low lateral resolution (e.g. Fig. 9D, E), stepping sills are imaged as oblique sheets. Also, because the impedance contrast between intrusives and host-rocks is so high, very little interference-effects between the layered host-rock and the oblique intrusions are observed. This is in contrast to modelling results reported previously lead to apparent steps (‘*pseudosteps*’) in the sill geometry in the seismic data, which were hypothesised to not be present in the subsurface (c.f. Magee et al 2015). This is almost opposite to the results we see in similar models. This is likely because the model employed in previous study employed 1D convolution, which dramatically overestimates horizontal resolution (c.f. Fig. 4, e.g. Magee et al 2015,). We therefore expect ‘pseudosteps’ to be of little importance, especially in seismic data below c. 1 km where horizontal resolution is low.

6.2.2 Noise

The simulated seismograms are generated without simulating acquisition noise. However, the simulated seismic images are not simply smoothed versions of the input models, but do contain several examples of discontinuous reflectors, dipping noise and amplitude variations which are not part of the input models, but that rather the results of simulation of diffractions occurring at discontinuities of reflectors. Fig 9E contains abundant examples of this.

In all models, the modelled reflections from the sill intrusions are coherent and show considerably stronger amplitudes than sedimentary reflectors. In all cases, even in Model D (Fig. 9E) which simulates imaging at 6 km depth, the reflections from the intrusives are detectable. In this case, the background seismic velocity is c. 4.6 km/s, the signal frequency is 10 Hz, and consequently, the wavelength of the signal is 465 m. This would mean that onset of tuning would occur at around 150 m, peak tuning would occur at 90 m, and onset of amplitude fall below the amplitude at no tuning would occur at 37 m. The sills in the study area are c. 10 m thick ($\lambda/47$), and would in this case give stronger reflections than an un-tuned sedimentary reflector. However, if acquisition noise was also modelled, would the intrusives be detectable? This is a difficult question to answer, because it is difficult to model acquisition noise in a rigorous manner (Scales and Snieder, 1998). The common way of adding noise to seismic sections could of course be performed, but the detectability of the reflections would depend on the amplitude of the noise, which would be entirely arbitrary because no good way of estimating the amplitude of noise in processed seismic data exists. Still, the modelling shows that as long as reflections from sedimentary interfaces are imaged, reflections from even relatively thin sills (more than a few meters) should be imaged as well.

6.3 Comparison to real data

A number of important issues are highlighted as the results from this study are compared to actual reflection seismic data.

6.3.1 Thickness and tuning

The vast majority of published examples of sill intrusions imaged in seismic data occur as tuned reflectors (e.g. Cukur et al., 2010; Schofield et al., 2012b; Haafez et al., 2017; Schmiedel et al., 2017), with a few exceptions where also the basal reflection is imaged separately (Hansen and Cartwright, 2006b; Jackson et al., 2013; Schofield et al., 2015). Commonly, these tuned reflections are interpreted to originate from sills that have thicknesses that lie close to the assumed tuning thickness of c. λ/4. However, the wedge model presented in Fig. 11, which models the seismic response to a reflection from a sediment-dolerite interface, indicates that a sill with a thickness of λ/11 should be capable of generating a reflection with the same amplitude as a sill with a thickness of λ/3. These results imply that the majority of mafic sill intrusions are relatively thin compared to seismic resolution, and is in accordance with datasets of thicknesses of drilled intrusions (Schofield et al., 2015). Also, tuned reflections should not simply be assumed to be close to the tuning thickness.

In deep and low-frequency seismic data, there is also the possibility that what is imaged as one reflector is in fact a reflection of several stacked sills, as in the example of Fig. 5F. This illustrates that seismic reflection data have the potential to significantly overestimate the thickness of discrete sills in a basin.

6.3.2 Un-imaged sills, and applications to seismic interpretation

The modelling and discussion above indicates that, theoretically, even thin sills should be possible to image in seismic reflection data, even at relatively deep (> 3 km's) basinal levels. However, many real world datasets combining well- and seismic data shows that large amounts of sills are in fact not imaged at all. For example, Schofield et al (2015) demonstrated that only a small number of the sills identified in well data from the Faroe-Shetland Basin are actually imaged in seismic data. A similar relationship can be seen in seismic data from the Vestbakken Volcanic Province at the western Barents Sea Margin (Figs. 1, 12). Exploration well 7317/5-1 encountered 12 sills which are clearly identifiable in wireline well logs (Fig. 12A, (Omosanya et al., 2016). These igneous intrusions make up an

652 upper and a lower sill complex. While the upper complex is relatively well imaged in seismic
653 data, the lower sill complex, consisting of intrusions ranging in thickness from 5 to 43 m, is
654 not imaged at all (Fig. 12B). There may be several reasons for this:

655 Although single continuous bodies of dolerite have a great potential for imaging, real sill
656 complexes do not consist of single continuous bodies, but rather several complex,
657 interconnected sills and thinner sill splays (e.g. Schofield et al., 2015, Eide et al., 2017; Fig.
658 13). In the case of thick sill complexes with large amounts of thin intrusions (c.f. Fig. 13E,
659 Schofield et al., 2015, their fig. 6B), seismic imaging will result in a strong reflection at the top
660 of the sill complex, as the average velocity and density increases. Below the top, reflections
661 from several thin intrusions interfere with each other, and yield no coherent reflections (Fig.
662 13E). Furthermore, although there is a strong acoustic impedance contrast at each sediment-
663 dolerite interface, these occur more closely spaced than seismic resolution, leading to
664 smaller effective impedance contrasts and therefore low seismic amplitudes.

665 Additionally, the lateral velocity structure can be highly variable through a sill complex (see
666 Fig. 13E). This means particular velocities used in migration are highly variable laterally, which
667 is not ideal when working with time migrated data, as imaging is often made worse by a poor
668 choice of velocity models, leading to migration artefacts which may fully mask underlying,
669 weaker reflection from sills.

670

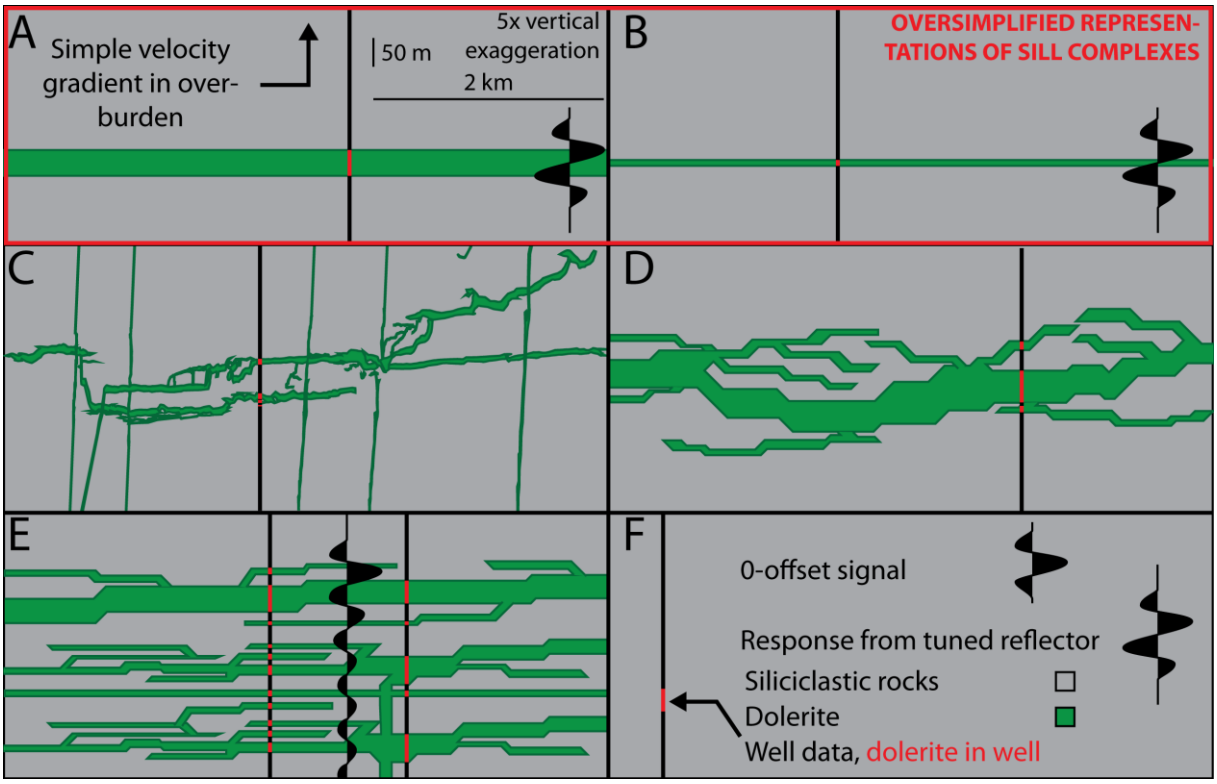

Fig 13: *Comparison of conceptual geometries of sill complexes, where individual sills are below seismic tuning thickness. A) Simple and unrealistic tabular sill, just below tuning thickness. B) Simple and unrealistic tabular sill, with a thickness of ¼ of the tuning thickness. Note that these are imaged at comparable amplitudes. C) Real-world example of a small- volume sill complex. D) A larger-volume sill-complex. Note large lateral variability in thickness and amount of dolerite. E) High-volume sill complex consisting of abundant thinner sills and splays. This example would likely give a strong reflection at the top, and weak and incoherent reflections below the top due to interference below seismic resolution. F) Legend.*

6.4 Future Perspectives

Considerable amounts of work have been done on the so-called 'sub-basalt imaging problem', which has yielded good results (c.f. Gallagher and Dromgoole, 2007). However, significantly more sedimentary basins contain extensive igneous sills, than large basaltic piles (e.g. South Australian Margin; Holford et al. 2012). Despite this, there is little awareness of issues relating to imaging of sill intrusions, and in particular imaging below sill complexes or the 'Sub-Sill Imaging Problem'. As accurate basin modelling relies on a good appreciation of source rock extent and thickness within a sedimentary basin, and given that in many sedimentary basins, potential source rock intervals (and occasional reservoirs) are inferred

689 to occur below sill complexes, it may be time to properly address the imaging issue and the
690 'Sub-Sill Imaging Problem'.

691 Importantly, synthetic seismic modelling presented in this paper indicates that relatively thin
692 igneous sills could potentially be imaged in reflection seismic data. However, inspection of
693 available datasets shows considerable migration artefacts below shallow intrusions, which
694 points towards poor representation of sills and geometries in velocity models. This is due to
695 the low thickness, high velocity, complex structure, and overall velocity changes that are
696 difficult to represent in velocity models. Depth migrated data is potentially better at
697 improving imaging, such data is only as good as the initial velocity model used, and that
698 model is only as good as the understanding of the sub-surface geology. Therefore,
699 improvement of this requires a greater understanding of where sills will appear in
700 sedimentary basins, better methods to predict architecture of sill complexes, , in order to
701 allow better informed velocity models to be attained. Until now, conceptual understanding
702 of sill complexes drawn from analysis of field data has only been applied for the
703 interpretation of seismic data. Such insights could also lay the foundations for progress in
704 processing and imaging and addressing of the 'sub-sill imaging problem'.

705 Imaging of igneous dykes is probably hampered by a lack of awareness of the importance of
706 these. Such discontinuous features, when viewed in a processing phase, may be simply
707 regarded as seismic artefacts and subsequently removed. This is a problem, as these can act
708 as significant barriers or conduits to hydrocarbons and other basinal fluids, depending on
709 post-emplacement evolution (e.g. Rateau et al. 2013; Senger et al., 2015; Eide et al., 2017).
710 Seismic modelling performed in this contribution indicates that these could potentially be
711 imaged in seismic data, and tentative interpretations of dykes have been made in regional
712 seismic lines (Minakov et al., 2017).

713

7. Conclusions

This study has investigated how mafic sill-complexes emplaced within sedimentary basins are imaged in reflection-seismic data at a variety of depths and under a variety of overburden conditions. This is important for seismic interpretation of sill complexes, which presents significant challenges for seismic interpretation, geologic forecasting and drilling. This has been done by generating synthetic seismograms using a 2D convolution method on a seismic-scale, sill-bearing outcrop-section from east Greenland, performing ray-based modelling to investigate lateral resolution at target depth for a variety of overburdens and target depths, and by comparing the synthetic seismograms to actual seismic. These are the main findings:

1) It is important to be aware of the illumination at the target depth, as low illumination leads to low maximum imaged dips and low lateral resolution will make it impossible to image steeply dipping features such as oblique dykes which might have important reservoir implications. 1D seismic convolution does not take horizontal resolution into account, and consistently overestimates horizontal resolution.
2) Igneous rocks, such as basalt flows or shallow intrusions, occurring between the imaging target and the seismic source and receivers will decrease vertical and particularly horizontal resolution at the target depth by absorbing high frequencies, seismic energy and diverting low-incidence seismic rays.
3) Commonly used rules-of-thumb for seismic detectability likely underestimate the minimum thickness of beds of mafic intrusions may be imaged in reflection seismic data because of the high acoustic impedance contrast between mafic intrusions and siliciclastic rocks.
4) The thickness of sills, either thick or thin, is no guarantee that they might be imaged. Migrated seismic data has the potential to image thin sills if the velocity models are good and sills are not so close that they interfere with each other
5) In reflection-seismic data of a reasonable quality, subseismic sill emplacement features such as splays, broken bridges and transgressive dykes may be inferred from sill geometries and amplitude variations.
6) Apparent steps in seismic data arising from interference between a layered host-rock and oblique dykes is likely not to occur in actual seismic data below c. 1 km depth because of limited horizontal resolution.

7) Improved imaging of sill complexes is important and may be achieved by integrating conceptual understanding of sill complexes and improved velocity models.

8. Acknowledgements

Funding for data collection was provided from the Research Council of Norway through the PETROMAKS project 193059 and the FORCE Safari project. Funding for data analysis and modelling was provided from PETROMAKS through the Trias North project (234152). The lidar data were acquired by Julien Vallet and Samuel Pitiot of Helimap Systems. We acknowledge NORSAR for an academic licence of the seismic modelling software *SeisRoX*, which was used to generate synthetic seismograms in this study, and NORSAR-2D, which was used for analysis of seismic propagation through the overburden models. We also acknowledge Tore Aadland for writing invaluable scripts used for import of the outcrop models to seismic modelling software, and Gijs A. Henstra and Björn Nyberg for assistance in the field.

9. References

Ahokas, J.M., Nystuen, J.P., and Martinius, A.W., (2014a) Depositional dynamics and sequence development of the paralic Early Jurassic Neill Klinter Group, Jameson Land Basin, East Greenland: Comparison with the Halten Terrace, mid-Norwegian continental shelf. In: From depositional systems to sedimentary successions on the Norwegian Continental Shelf (Eds A. W. Martinius, R. Ravnås, J. A. Howell, R. J. Steel, and J. P. Wonham), Int. Assoc. Sedimentol. Spec. Publ. 46, 291-333.

Baig, I., Faleide, J. I., Jahren, J., & Mondol, N. H. (2016). Cenozoic exhumation on the southwestern Barents Shelf: Estimates and uncertainties constrained from compaction and thermal maturity analyses. Marine and Petroleum Geology, 73, 105-130.

Brooks, C.K., (1973). Rifting and doming in southern East Greenland. Nat. Phys. Sci. 244, 23–24.

Brooks, C. K. (2011). The East Greenland rifted volcanic margin. Geological Survey of Denmark and Greenland Bulletin, 24, 96.

Brown, A. R. (2011). Interpretation of three-dimensional seismic data. Society of Exploration Geophysicists and American Association of Petroleum Geologists.

Bryan, S. E., & Ferrari, L. (2013). Large igneous provinces and silicic large igneous provinces: Progress in our understanding over the last 25 years. Geological Society of America Bulletin, 125(7-8), 1053-1078.

Buckley, S.J., Vallet, J., Braathen, A. and Wheeler, W. (2008) Oblique helicopter-based laser scanning for digital terrain modelling and visualization of geological outcrops. Int Arch Photogrammetry, Remote Sens Spatial Inform Sci, 37, 493–498.

Cartwright, J and Hansen, D.M. (2006b) Magma transport through the crust via interconnected sill complexes. Geology, 31, 929-932.

Cartwright, J., & Huuse, M. (2005). 3D seismic technology: the geological 'Hubble'. Basin Research, 17, 1-20.

Cukur, D., Horozal, S., Kim, D. C., Lee, G. H., Han, H. C., & Kang, M. H. (2010). The distribution and characteristics of the igneous complexes in the northern East China Sea

789 Shelf Basin and their implications for hydrocarbon potential. Marine Geophysical Researches,
790 31(4), 299-313.

791 Dam, G. and Surlyk, F. (1998) Stratigraphy of the Neill Klinter Group; a Lower – lower
792 Middle Jurassic tidal embayment succession, Jameson Land, East Greenland. Geology of
793 Greenland Survey Bulletin, 175, 80 pp.

794 Eide, C. H., Howell, J. A., Buckley, S. J., Martinius, A. W., Oftedal, B. T., & Henstra, G. A.
795 (2016). Facies model for a coarse-grained, tide-influenced delta: Gule Horn Formation (Early
796 Jurassic), Jameson Land, Greenland. Sedimentology, 63(6), 1474-1506.

797 Eide, C. H., Schofield, N., Jerram, D. A., & Howell, J. A. (2017). Basin-scale architecture of
798 deeply emplaced sill complexes: Jameson Land, East Greenland. Journal of the Geological
799 Society, 174(1), 23-40.

800 Eldhom, O., & Coffin, M. F. (2000). Large igneous provinces and plate tectonics. The history
801 and dynamics of global plate motions, 309-326.

802 Faleide, J. I., Tsikalas, F., Breivik, A. J., Mjelde, R., Ritzmann, O., Engen, O., Wilson, J., &
803 Eldholm, O. (2008). Structure and evolution of the continental margin off Norway and the
804 Barents Sea. Episodes, 31(1), 82-91.

805 Flecha, I., Carbonell, R., Hobbs, R. W., & Zeyen, H. (2011). Some improvements in subbasalt
806 imaging using pre-stack depth migration. Solid Earth, 2(1), 1.

807 Gallagher, J. W., & Dromgoole, P. W. (2007). Exploring below the basalt, offshore Faroes: a
808 case history of sub-basalt imaging. Petroleum Geoscience, 13(3), 213-225.

809 Galland, O. (2012). Experimental modelling of ground deformation associated with shallow
810 magma intrusions. Earth and Planetary Science Letters, 317, 145-156.

811 Galland, O., Planke, S., Neumann, E.-R., Malthe-Sørenssen, A. (2009) Experimental modelling
812 of shallow magma emplacement: Application to saucer-shaped intrusions. Earth Planet. Sci.
813 Lett., 277, 373-383 .

814 Gjøystdal, H., Iversen, E., Lecomte, I., Kaschwich, T., Drottning, Å., & Mispel, J. (2007).
815 Improved applicability of ray tracing in seismic acquisition, imaging, and interpretation.
816 Geophysics, 72(5), SM261-SM271.

817 Hafeez, A., Planke, S., Jerram, D. A., Millett, J. M., Maharjan, D., & Prestvik, T. (2017). Upper
818 Paleocene ultramafic igneous rocks offshore mid-Norway: Reinterpretation of the Vestbrona
819 Formation as a sill complex. Interpretation, 5(3), SK103-SK120.

820 Hald, N. and Tegner, C. (2000) Composition and age of tertiary sills and dykes, Jameson
821 Land Basin, East Greenland: relation to regional flood volcanism. Lithos, 54, 207-233.

822 Hansen D.M. and Cartwright, J. (2006a). Saucer-shaped sill with lobate morphology revealed
823 by 3D seismic data: implications for resolving a shallow-level sill mechanism. J. Geol. Soc.
824 London, 163, 509-523.

825 Hansen, D. M., & Cartwright, J. (2006b). The three-dimensional geometry and growth of
826 forced folds above saucer-shaped igneous sills. Journal of Structural Geology, 28(8), 1520-
827 1535.

828 Henriksen, E., Bjørnseth, H. M., Hals, T. K., Heide, T., Kiryukhina, T., Kløvjan, O. S., Larssen,
829 G. B., Ryseth, A. E., Rønning, K., Sollid, K & Stoupakova, A. (2011). Uplift and erosion of the
830 greater Barents Sea: impact on prospectivity and petroleum systems. Geological Society,
831 London, Memoirs, 35(1), 271-281.

832 Hersum, T.G., Marsh, B.D., and Simon A.C. (2007). Contact Partial Melting of Granitic
833 Country Rock, Melt Segregation, and Re-injection as Dikes into Ferrar Dolerite Sills,
834 McMurdo Dry Valleys, Antarctica. J. Petrology (2007) 48 (11): 2125-2148.

835 Holford, S.P., Schofield, N., Jackson, C.A.-L., Magee, C., Green, P.F., and Duddy, I.R. (2013)
836 Impacts of Igneous Intrusions on Source and Reservoir Potential in Prospective Sedimentary
837 Basins along the Western Australian Continental Margins. In: West Australian Basins
838 Symposium, pp. 1-12.

839 Holford, S., Schofield, N., MacDonald, J., Duddy, I., & Green, P. (2012). Seismic analysis of
840 igneous systems in sedimentary basins and their impacts on hydrocarbon prospectivity:
841 Examples from the southern Australian margin. The APPEA Journal, 52(1), 229-252.

842 Hutton, D.H.W. (2009) Insights into magmatism in volcanic margins: bridge structures and a
843 new mechanism of basic sill emplacement - Theron Mountains, Antartica. Petroleum
844 Geoscience, 15, 269-278.

845 Ichaso, A.A. and Dalrymple, R.W. (2014) Eustatic, tectonic and climatic controls on an early
846 syn-rift mixed-energy delta, Tilje Formation (Early Jurassic, Smørbukk field, offshore mid-
847 Norway). In: From Depositional Systems to Sedimentary Successions on the Norwegian
848 Continental Margin (Eds A. W. Brooks, R. Ravnås, J. A. Howell, R. J. Steel and P. Wonham),
849 IAS Spec. Publ 46, 339-388.

850 Jackson, C. A., Schofield, N., & Golenkov, B. (2013). Geometry and controls on the
851 development of igneous sill–related forced folds: A 2-D seismic reflection case study from
852 offshore southern Australia. Geological Society of America Bulletin, 125(11-12), 1874-1890.

853 Jerram, D.A. & Bryan, S. E. 2015. Plumbing Systems of Shallow Level Intrusive Complexes.
854 Part of the series Advances in Volcanology pp 1-22, Springer.

855 Jerram, D.A., Davis, G.R., Mock, A., Charrier, A., and Marsh, B.D. (2010). Quantifying 3D
856 crystal populations, packing and layering in shallow intrusions: a case study from the
857 Basement Sill, Dry Valleys, Antarctica. GEOSPHERE Volume: 6 Issue: 5 Pages: 5

858 Kallweit, R. S., & Wood, L. C. (1982). The limits of resolution of zero-phase wavelets.
859 Geophysics, 47(7), 1035-1046.

860 Lecomte, I., Lavadera, P. L., Botter, C., Anell, I., Buckley, S. J., Eide, C. H., Grippa, A.,
861 Mascolo, V. and Kjoberg, S. (2016). 2 (3) D convolution modelling of complex geological
862 targets beyond 1D convolution. First Break, 34, 99-107.

863 Lecomte, I., Lavadera, P. L., Anell, I., Buckley, S. J., Schmid, D. W., & Heeremans, M. (2015).
864 Ray-based seismic modeling of geologic models: Understanding and analyzing seismic images
865 efficiently. Interpretation, 3(4), SAC71-SAC89.

866 Magee, C., Maharaj, S. M., Wrona, T., & Jackson, C. A. L. (2015). Controls on the expression
867 of igneous intrusions in seismic reflection data. Geosphere, 11, 1024-1041.

868 Magee, C., Hunt-Stewart, E., & Jackson, C. A. L. (2013). Volcano growth mechanisms and the
869 role of sub-volcanic intrusions: Insights from 2D seismic reflection data. Earth and Planetary
870 Science Letters, 373, 41-53.

871 Larsen, H.C. and Marcussen, C. (1992) Sill-intrusion, flood basalt emplacement and deep
872 crustal structure of the Scoresby Sund Region, East Greenland. In: Magmatism and the

873 Causes of Continental Break-up (Eds B.C. Storey, T. Alabaster and R.J. Pankhurst),
874 Geological Society Special Publication, 68, 365-368.

875 Martinius, A.W., Kaas, I., Næss, A., Helgesen, G, Kjærefjord, J.M. and Leith, D.A. (2001)
876 Sedimentology of the heterolithic and tide-dominated Tilje Formation (Early Jurassic, Halten
877 Terracce, offshore mid-Norway). In: Sedimentary Environments Offshore Norway -
878 Palaeozoic to Recent (Eds O. J. Martinsen and T. Dreyer) NPF Special Publication 10, 103-
879 144.

880 Mathiesen, A., Bidstrup, T., Christiansen, F.G. (2000) Denudation and uplift history of the
881 Jameson Land basin, East Greenland - constrained from maturity and apaite fission track
882 data. Global and Planetary Change, 24, 275-301.

883 Millett, J. M., Wilkins, A. D., Campbell, E., Hole, M. J., Taylor, R. A., Healy, D., Jerram, D. A.,
884 Jolley, D. W., Planke, S., Archer, S. G., & Blischke, A. (2016). The geology of offshore drilling
885 through basalt sequences: Understanding operational complications to improve
886 efficiency. Marine and Petroleum Geology, 77, 1177-1192.

887 Minakov, A., Yarushina, V., Faleide, J. I., Krupnova, N., Sakoulina, T., Dergunov, N., &
888 Glebovsky, V. (2017). Dyke emplacement and crustal structure within a continental large
889 igneous province, northern Barents Sea. Geological Society, London, Special Publications,
890 460, SP460-4.

891 Muirhead, J. D., Van Eaton, A. R., Re, G., White, J. D., & Ort, M. H. (2016). Monogenetic
892 volcanoes fed by interconnected dikes and sills in the Hopi Buttes volcanic field, Navajo
893 Nation, USA. Bulletin of Volcanology, 78(2), 1-16.

894 Muirhead, D.K., Bowden, S.A., Parnell, J. & Schofield, N. (*in press)*. Muirhead, Source rock
895 maturation owing to igneous intrusion in rifted margin petroleum systems. Journal of the
896 Geological Society

897 Omosanya, K. O., Johansen, S. E., & Abrahamson, P. (2016). Magmatic activity during the
898 breakup of Greenland-Eurasia and fluid-flow in Stappen High, SW Barents Sea. Marine and
899 Petroleum Geology, 76, 397-411.

900 Planke, S., Rasmussen, T., Rey, S.S., and Myklebus, R. (2005) Seismic characteristics and
901 distribution of volcanic intrusions and hydrothermal vent complexes in the Vøring and Møre

902 basins. In: Petroleum Geology: North-West Europe and Global Perspectives—Proceedings
903 of the 6th Petroleum Geology Conference (Eds A. G. Dore and B. A. Vining), 833-844

904 Rateau, R., Schofield, N., & Smith, M. (2013). The potential role of igneous intrusions on
905 hydrocarbon migration, West of Shetland. Petroleum Geoscience, 19(3), 259-272.

906 Rittersbacher, A., Buckley, S. J., Howell, J. A., Hampson, G. J. and Vallet J. (2013) Helicopter-
907 based laser scanning: a method for quantitative analysis of large-scale sedimentary
908 architecture. In: Sediment-Body Geometry and Heterogeneity: Analogue Studies for
909 Modelling the Subsurface (Eds A. W. Martinius, J.A. Howell and T. Good), Geol. Soc. London
910 Spec. Publ. 238

911 Saunders, A. D., Fitton, J. G., Kerr, A. C., Norry, M. J. and Kent, R. W. (1997). The North
912 Atlantic Igneous Province. Geophysical Monograph 100, 45–93.

913 Scales, J. A., & Snieder, R. (1998). What is noise?. Geophysics, 63(4), 1122-1124.

914 Schmiedel, T., Kjoberg, S., Planke, S., Magee, C., Galland, O., Schofield, N., Jackson, C. A.-K.,
915 & Jerram, D. A. (2017). Mechanisms of overburden deformation associated with the
916 emplacement of the Tulipan sill, mid-Norwegian margin. Interpretation, 5(3), SK23-SK38.

917 Schofield, N.J., Brown, D.J., Magee, C., and Stevenson, C.T. (2012a) Sill morphology and
918 comparison of brittle and non-brittle emplacement mechanisms. J. Geol. Soc. 169, 127-141.

919 Schofield, N., Holford, S., Millett, J., Brown, D., Jolley, D., R Passey, S., Muirhead, D., Grove,
920 C., Magee, C., Murray, J. and Hole, M., (2015). Regional magma plumbing and emplacement
921 mechanisms of the Faroe-Shetland Sill Complex: implications for magma transport and
922 petroleum systems within sedimentary basins. Basin Research.

923 Schofield N, Jerram, D.A., Holford, S., Archer, S., Mark, N., Hartley, A., Howell, J.A.,
924 Muirhead, D., Green, P., Hutton, D., Stevenson, C. (2016). Sills in sedimentary basins and
925 petroleum systems. Advances in Volcanology, Springer Berlin Heidelberg (in press)

926 Schofield, N., Jolley, D., Holford, S., Archer, S., Watson, D., Hartley, A., Howell, J., Muirhead,
927 D., Underhill, J & Green, P. (2017). Challenges of future exploration within the UK Rockall
928 Basin. In Geological Society, London, Petroleum Geology Conference series (Vol. 8, pp.
929 PGC8-37). Geological Society of London.

930 Schofield, N., Heaton, L., Holford, S.P, Archer, S.G., Jackson, C.A.-L and Jolley, D.W. (2012b)
931 Seismic imaging of 'broken bridges': linking seismic to outcrop-scale investigations of
932 intrusive magma lobes. J. Geol. Soc. London, 169, 421-426.

933 Schofield, N., Stevenson, C., and Reston, T. (2010) Magma fingers and host rock fluidization
934 in the emplacement of sills. Geology, 38, 63-66.

935 Senger, K., Buckley, S. J., Chevallier, L., Fagereng, Å., Galland, O., Kurz, T. H., Ogata, K.,
936 Planke, S. & Tveranger, J. (2015). Fracturing of doleritic intrusions and associated contact
937 zones: implications for fluid flow in volcanic basins. Journal of African Earth Sciences, 102,
938 70-85.

939 Senger, K., Millett, J., Planke, S., Ogata, K., Eide, C. H., Festøy, M., Galland, O., & Jerram, D.
940 A. (2017) Effects of igneous intrusions on the petroleum system: a review. First Break, 35.

941 Sheriff, R. E. and Geldart, L. P. (1995). Exploration Seismology (2nd Edn). Cambridge
942 University Press. 628 p.

943 Simm, R., & Bacon, M. (2014). Seismic Amplitude: An interpreter's handbook. Cambridge
944 University Press.

945 Skogseid, J., Planke, S., Faleide, J. I., Pedersen, T., Eldholm, O., & Neverdal, F. (2000). NE
946 Atlantic continental rifting and volcanic margin formation. Geological Society, London,
947 Special Publications, 167(1), 295-326.

948 Smallwood, J. R., & Maresh, J. (2002). The properties, morphology and distribution of
949 igneous sills: modelling, borehole data and 3D seismic from the Faroe-Shetland area.
950 Geological Society, London, Special Publications, 197(1), 271-306.

951 Surlyk, F. (2003) The Jurassic of East Greenland: a sedimentary record of thermal
952 subsidence, onset and culmination of rifting. In: The Jurassic of Denmark and Greenland (Eds.
953 J. R. Ineson and F. Surlyk), Geological Survey of Denmark and Greenland Bulletin, 1, p. 659-
954 722.

955 Svensen, H., Polteau, S., Cawthorn, G., and Planke, S. (2015) Sub-volcanic intrusions in the
956 Karoo Basin, South Africa. Advances in Volcanology. In Press. DOI: 10.1007/11157_2014_7

957 Talwani, M., & Eldholm, O. (1977). Evolution of the Norwegian-Greenland sea. Geological
958 Society of America Bulletin, 88(7), 969-999.

959 Thomson, K., & Hutton, D. (2004). Geometry and growth of sill complexes: insights using
960 3D seismic from the North Rockall Trough. Bulletin of Volcanology, 66(4), 364-375.

961 Thomson, K., & Schofield, N. (2008). Lithological and structural controls on the
962 emplacement and morphology of sills in sedimentary basins. Geological Society, London,
963 Special Publications, 302(1), 31-44.

964 Vallet, J., & Skaloud, J. (2004). Development and experiences with a fully-digital handheld
965 mapping system operated from a helicopter. The International Archives of the
966 Photogrammetry, Remote Sensing and Spatial Information Sciences, Istanbul, 35 (Part B).

967 van Cappelle, M., Ravnås, R., Hampson, G. J., & Johnson, H. D. (2017). Depositional evolution
968 of a progradational to aggradational, mixed-influenced deltaic succession: Jurassic Tofte and
969 Ile formations, southern Halten Terrace, offshore Norway. Marine and Petroleum Geology,
970 80, 1-22.

971 Ziolkowski, A., Hanssen, P., Gatliff, R., Jakubowicz, Li, X.-Y., Jakubowicz, H & Hampson, G.
972 (2003). Use of low frequencies for sub-basalt imaging. Geophysical Prospecting, 51(3), 169-
973 182.

974

975 # 11. Tables

976

977 Table 1: Input data for modeling. NCS, Norwegian Continental Shelf; MD, measured depth.

a) Values for target at 1 and 3 km depth

Name	Facies association	V_P	V_P/V_S	Density	Source	Depth
	#	*km/s*	*fraction*	*g/cm3*	*NCS well/article*	*MD (m)*
Igneous intrusions	1	6,3	1,86	3,0	Smallwood and Maresh, 2002	
Homogeneous sandstone	2	3,7	1,80	2,5	Add 5% to FA3	-
Sandstone	3	3,5	1,80	2,4	6407/2-1	3220-3235
Poorly cemented sandstone	4	3,4	1,80	2,3	Subtract 5% FA3	-
Heterolithic	5	3,3	1,80	2,3	6407/2-1	3030-3050
Mudstone	6	3,8	1,80	2,5	6407/2-1	2920-2940
Organic rich mudstone	7	2,6	1,80	2,3	6407/2-1	2885-2900

b) Values for target at 6 km depth

Igneous intrusions	1	6,3	1,86	3,0	Smallwood and Maresh, 2002	
Homogeneous sandstone	2	4,8	1,80	2,7	Add 5% to FA3	-
Sandstone	3	4,6	1,80	2,6	6506/12-10A	5525-5545m
Poorly cemented sandstone	4	4,4	1,80	2,4	Subtract 5% FA3	-
Heterolithic	5	4,7	1,80	2,5	6506/12-10A	5565-5582m
Mudstone	6	4,7	1,80	2,4	6506/12-10A	5618-5635m
Organic rich mudstone	7	3,9	1,80	2,5	6506/12-10A	5330-5335m

978